MICROMACHINED ACOUSTIC DELAY LINE TECHNOLOGIES

FOR PHOTOACOUSTIC SENSING APPLICATIONS

A Dissertation

by

ARIF KIVANC USTUN

Submitted to the Office of Graduate and Professional Studies of
Texas A&M University
in partial fulfillment of the requirements for the degree of

DOCTOR OF PHILOSOPHY

Chair of Committee,	Jun Zou
Committee Members,	Pao-Tai Lin
	Raffaella Righetti
	Sheng-Jen Hsieh
Head of Department,	Miroslav M. Begovic

May 2021

Major Subject: Electrical Engineering

ABSTRACT

Photoacoustic sensing (PAS) has been used for a number of biomedical applications, which take the advantage of rich optical absorption contrast and deep acoustic penetration depth in tissues. However, current PAS devices are bulky, invasive, and susceptible to interference during excitation. In the thesis, miniaturized PAS probes based on acoustic delay lines (ADLs) are studied. First, a compact two-optical-fiber PAS probe is designed, fabricated, and tested. It consists of one optical fiber for light delivery and the other one for relaying the generated photoacoustic (PA) signal from the target to an outside ultrasound transducer (UTX). With the addition of a suitable time delay, the PA signal can be easily separated from the interference signals. Secondly, to create an even more compact structure, a PAS probe design using a single optical fiber for both light delivery and PA detection is investigated. An optically transparent UTX is developed, which allows the excitation light to pass through and at the same time detect the generated PA signal transmitted through the optical fiber as an ADL. Thirdly, to improve the frequency response of PA detection, a new PAS probe based on silicon acoustic delay lines (SADLs) is explored to replace the fused-silica optical fibers. Compared with fused-silica, single-crystalline silicon has much higher acoustic velocity and lower acoustic attenuation and can therefore support non-dispersive acoustic transmission at much higher frequencies. Lastly, a high-frequency SADL array is demonstrated to enable simultaneous multi-channel PA detection. The multi-channel detection capabilities can also be useful for PA imaging applications.

DEDICATION

To my wife and unborn baby,

To the great leader and founder of modern Turkey, Mustafa Kemal Ataturk, who provides a unique opportunity for students like me to complete their graduate studies abroad since 1929.

"*Science is the only true guide in life*", Ataturk

ACKNOWLEDGEMENTS

First of all, I would like to thank my committee chair, Dr. Jun Zou. This work would not have been possible without his profound guidance throughout my entire Ph.D. study. He has always provided scientific guidance showing different perspectives and given me precious spirit and strength.

I would like to thank my committee members, Professors Pao-Tai Lin, Rafaella Righetti, and Tony "Sheng-Jen" Hsieh for their support during this research.

I am grateful to all of my colleagues, Cheng Fang, Dr. Young Cho, Dr. Song Xu, Akhil Kumar, Zhiyu Yan, Shuangliang Li, Zijie Zhao, Xiaoyu Duan, Ju Ong, who all supported me by selflessly sharing research experiences and knowledge whenever I need.

I want to extend my appreciation to the technical staff of the AggieFab, Mr. Larry Rehn, Mr. Robert Atkins, Mr. Don Marek, Dr. Ming-Wei Lin, Mr. Jung-Hwan Woo, Mr. Ethan Morse, and Mr. Mitchell Roselius. They maintained a good working environment and facility, and also provided me the essential trainings.

Most importantly, I wish to thank my dear wife, Meltem, who is also doing her Ph.D. here and has been always supportive. Last but not least, thanks to my parents for their unending supports and encouragement during this journey.

CONTRIBUTORS AND FUNDING SOURCES

Contributors

This work was supervised by a dissertation committee consisting of Professors Jun Zou, Pao-Tai Lin and Raffaella Righetti of the Department of Electrical and Computer Engineering, and Professor Tony “Sheng-Jen” Hsieh of the Department of Engineering Technology & Industrial Distribution at the Texas A&M University.

Funding Sources

This work was partially supported by the Ministry of National Education, Turkey. This work also made possible in part by the National Science Foundation under Grant Number CMMI-1131758 and ECCS-1809710. Its contents are solely the responsibility of the authors and do not necessarily represent the official views of the National Science Foundation.

NOMENCLATURE

ADL	Acoustic Delay Line
ADF	Acoustic Delay Fiber
ANSI	American National Standard Institute
DAQ	Data Acquisition
FFT	Fast-Fourier Transform
Nd:YAG	Neodymium-doped Yttrium Aluminum Garnet
PA	Photoacoustics
PAS	Photoacoustic Sensing
PAT	Photoacoustic Tomography
PCB	Printed Circuit Board
PZT	Lead Zirconate Titanate
RIE	Reactive Ion Etching
SADL	Silicon Acoustic Delay Line
SNR	Signal-to-Noise Ratio
UTX	Ultrasound Transducer

TABLE OF CONTENTS

Page

LIST OF FIGURES

Page

LIST OF TABLES

Page

1. INTRODUCTION

1.1. Motivation

Recently, photoacoustics (PA) is gaining more and more interests in the field of biomedical sensing and imaging. For photoacoustic sensing (PAS), short (nanosecond) laser pulses are delivered and absorbed inside the tissue (target), which generate ultrasound waves (i.e., PA waves). The peak amplitude and travel time of the PA signals can be used to retrieve the concentration and location of the (optical) absorbers in the target. A fundamental challenge in the PAS system design is how to optimize the optical delivery and acoustic detection schemes for obtaining the best sensing performances. Although various PAS probes have been developed, few efforts have been focused on the miniaturization for creating compact structures with minimal invasiveness for *in-vivo* use.

In PAS, the light delivery and acoustic detection need to be conducted in close proximity to the target to reduce optical and acoustic divergence and attenuation inside the tissue. However, with the ultrasound transducer (UTX) placed close to the target, the PA signal will arrive at the transducer within a very short period of time. Therefore, it could be easily buried under the much stronger interference signals occurring at each PA excitation. This situation makes the extraction, processing, and interpretation of the PA data rather difficult. This issue can be addressed by using a wire-type acoustic delay line (ADL) to relay the generated PA signal from the target to an outside UTX while creating a desirable amount of acoustic time delay. With the added acoustic time delay, the PA signal will arrive at the transducer after the interference signals diminish and therefore can

be easily distinguished in the time domain. Furthermore, with the transducer located outside, a small probe diameter can be achieved to minimize its invasiveness for *in-vivo* use. In this work, the acoustic transmission properties of ADLs made of optical fibers and single-crystalline silicon are experimentally characterized. Their applications in PAS probe designs are investigated.

1.2. Summary of Work

The dissertation has been organized in the following way:

In Section 2, the principle of the PA effect and the previous works on PAS probes are reviewed. Next, the fundamental principle of ADLs is reviewed. The relationship between their acoustic performances vs. material properties and geometric parameters are discussed.

In Section 3, a new PAS probe design based on two optical fibers is presented, with one fiber for light delivery and the second fiber as an ADL for PA detection/transmission. This design allows a compact probe structure with clear PA signal separation from interferences to be achieved. For demonstration, a prototype probe was fabricated and tested. Both ultrasound and PA characterization have been conducted with different target materials and depths.

In Section 4, a new PAS probe design based on a single optical fiber is presented to provide an even more compact probe structure. The single optical fiber serves as both an optical waveguide and an ADL for simultaneous light delivery and acoustic detection, respectively. It is made possible by the development and use of an optically transparent UTX. With the single-fiber approach, a good overlap between optically radiated region

and acoustic detection in the tissue was maintained, leading to better sensitivity compared to the two-fiber PAS probe. For demonstration, a prototype probe was also fabricated and tested.

In Section 5, silicon acoustic delay lines (SADLs) are first investigated to achieve much higher non-dispersive transmission frequencies where optical fiber ADLs underperform. Next, a new PAS probe design based on SADLs is presented, which consists of one optical fiber for light delivery, two SADLs for acoustic detection/transmission, and a high-frequency UTX. Micro linkers are designed and fabricated by high-resolution 3D printing to provide necessary mechanical protection and acoustic isolation for the SADLs. Both ultrasound and PA testing are conducted to verify the improved frequency response of the PAS probe.

In Section 6, a new micromachined SADL design for transmitting high-frequency ultrasound signals with different time delays is presented. Novel thin-film backside linkers are investigated to address the structural instability issue without affecting the acoustic performance. High-frequency ultrasound transmission through a multi-channel SADL array has been demonstrated. The new high-frequency SADL design is expected to enable multi-channel PAS capability at high frequencies.

2. BACKGROUND AND LITERATURE REVIEW

2.1. Photoacoustic (PA) Effect

Light-induced acoustic wave generation, also called the photoacoustic (PA) effect was first discovered by Alexander Graham Bell in 1880 [1, 2]. During the last three decades, the PA effect has been utilized for sensing or imaging optically absorptive targets in biological tissues beyond the (soft) optical diffraction depth limit [3-5]. PA sensing and imaging combines rich optical absorption contrast and good acoustic penetration depth [6, 7]. Specific tissues having a higher probability of photon energy absorption (compared to tissues nearby) [8] such as blood vessels [9], tumors [10, 11], and lesions [12] comprise greater optical absorption. A few examples of proper endogenous/exogenous contrast agents for PA applications are different states of materials, gases, liquids, and solids [13], various high contrast materials in human skin, e.g. hemoglobin, melanin, bilirubin, and carotene [14, 15], and nanoparticles such as gold nanostructures [16, 17], dyes [18], and polymer nanoparticles [19, 20]. In such cases, the absorbing capability of each contrast agent strongly depends on the wavelength. For instance, the aforementioned absorbers are typically effective at visible wavelengths while glucose [21, 22] and lipids [13, 23] absorb the photons more effectively in the near-infrared/mid-infrared region.

2.2. PA Wave Generation

PA effect can be used to address many discriminative analyses among tissues [24]. It is typically defined as a combination of absorbed electromagnetic radiation energy and detected ultrasonic waves converted within biological tissues/media. Indeed, the PA wave

generation mechanism mainly depends on several consecutive steps that physically occur in the tissue [25, 26]. A short-pulsed (nano-second) laser supplies monochromatic (single-wavelength) light, which illuminates the tissue. Depending on the optical absorption coefficient of the tissue, the absorbed energy is converted into heat. The temperature of the heated molecules rises, which originates the transient thermal expansion. In a very short amount of time (more than 3-4 order of magnitude less than a second), the thermal expansion occurs and followed by shrinking molecules in a rapid fashion. The pressure changes are inherently a consequence of the thermal expansion in the molecules, and then the periodical changes generate mechanical vibrations called ultrasound waves or PA waves depends on the existence of a light/laser excitation.

PA wave generation is key to understand the concept of PAS. Instead of continuous wave (CW) lasers, short-pulsed lasers have been used due to their better signal-to-noise ratio (SNR) (> 20-30 dB, much stronger at high frequencies) [27, 28]. After the absorbers are irradiated by the lasers, the optical energy transforms into thermal energy [8]. This thermal energy creates a pressure rise via thermoelastic expansion so that the propagation of PA wave can be defined as

$$\left(\nabla^2 - \frac{1}{\upsilon_s^2}\frac{\partial}{\partial t^2}\right) p(\vec{r},t) = -\frac{\beta}{C_p}\frac{\partial H(\vec{r},t)}{\partial t} \qquad (2.1)$$

where $p(\vec{r},t)$ denotes PA wave at position r and time t, υ_s is the sound velocity (m/s), β is thermal expansion coefficient (K^{-1}), C_p is the heat capacity at constant pressure (J/gK), and $H(\vec{r},t)$ denotes the heating function. The propagation of PA waves can be described by using the first derivative of the heating function, $H(\vec{r},t)$. Therefore, the generated PA

waves exist when there is time-variant heating [29, 30]. The relationship between the initial pressure rise for a delta-pulse excitation and the heating function can be defined in the heated region of the tissue:

$$\Delta P = \Gamma \, n_{th} \, F \, \mu_a \tag{2.2}$$

where ΔP is initial pressure rise, Γ is Grüneisen parameter (dimensionless), n_{th} is the heat conversion ratio, F is the laser fluence (mJ/cm^2), and μ_a is the absorption coefficient of the medium (cm^{-1}). The pressure rise in the irradiated tissue typically depends on the conversion efficiency from the thermal energy to the pressure (related to Γ), the ratio of absorbed photon energy which is converted to heat (related to n_{th}), the number of absorbers per unit target (related to μ_a), and the optical fluence (F). Derived from the pressure rise, the detection sensitivity of the generated PA waves can be increased. Also, the Grüneisen parameter is defined as

$$\Gamma = \beta \upsilon_s \Big/ C_p \ . \tag{2.3}$$

This shows that the materials having high sound velocity, e.g., silicon or silica, can therefore be a good candidate for transmission of the generated PA signals. Moreover, a short-pulsed laser with moderate power would be a safe permissible exposure to supply optical power for living tissues [31]. There is accordingly another limitation related to maximum laser fluence in biomedical applications, which is called the American National Standards Institute (ANSI) limit. It is described for a short-pulsed laser light (1-100ns) with a visible wavelength (400-700 nm) to be $20mJ/cm^2$ and $100mJ/cm^2$ for 700-1400 nm [32].

For optimum parameters of a qualitative PA sensing and imaging, high sensitivity, deep penetration depth, low acoustic attenuation, high-frequency, wide bandwidth, and high resolution are the parameters with tradeoffs to consider in the biomedical imaging applications [3, 33].

The sensitivity of a PAS system can be measured with a minimum detectable signal. The smaller minimum detectable signal is an indicator of higher sensitivity in the system. Attaining high sensitivity, while taking into account the generation of PA waves, is explained above by altering the parameters of the rise in pressure (ΔP).

Penetration depth is defined as how deep light waves can penetrate into a tissue. The penetration depth of PA sensing and imaging in tissues is still limited by the maximal allowable laser fluence (proportional to F), the optical absorption (μ_a), and acoustic attenuation. It is also dependent upon the detection bandwidth of UTX [8, 34].

The acoustic detection depends on the acoustic properties of the target material such as ultrasound scattering and acoustic attenuation [35, 36]. Different than optical tomography/microscopy, the PA system exploits the advantage that ultrasonic scattering is much less than optical scattering [37, 38]. More importantly, acoustic attenuation is a phenomenon that is inversely proportional to the frequency. In tissues, this phenomenon turns into a quadratic relationship [39]. Hence, acoustic attenuation degrades signal quality, i.e. reduction in amplitude and broadening of the pulse length [40], which worsens both the axial resolution and the lateral resolution. Besides, lower penetration depth has been received within the high-frequency PA testing setup because smaller wavelengths travel through shallow regions and attenuate stronger than longer wavelength signals in

the tissue [41]. In other words, it is still difficult to detect a target buried deeply inside the tissue with good contrast at higher frequencies or smaller wavelengths.

While acoustic attenuation affects the bandwidth of the PA signals, other factors also change the bandwidth such as laser pulse's length and shape [7] as well as the size and shape of the absorbers. Correspondingly the detection bandwidth of a UTX limits the bandwidth of the generated PA signal [36, 42], but broadband transducers will be operated to receive sensitive detection. Broadband transducers are useful to detect the PA signals from a large bandwidth since it combines the advantages of high/low-frequency components, high spatial resolution, and deep penetration depth.

2.3. Conventional PAS Probes

Guided biopsy needles [43-46], contact-based PAS probes [47-49], PA endoscopes [50-52], or intravascular PA imaging devices [53-55] have been previously developed to conduct localized measurements (Figure 2-1). For example, the needle-based devices are based on the optical absorption differences for detecting needles (or specific absorbers) within the imaging field of view [43, 56, 57] (Figure 2-1a). Imaging of metal needles [58] due to higher optical absorption compared to the tissue nearby may be useful for real-time guidance biopsy applications [44]. Although other PA or ultrasound probes use optical fibers for light delivery, the PAS probes are used to detect generated PA or ultrasound signals based on optical sensing approaches, e.g., high finesse, transparent, or tunable Fabry-Perot cavity [56, 59, 60]. As another "light delivery-ultrasound detection" PAS probe design (Figure 2-1b), namely contact-based probes, three optical fibers are built within a probe for a minimally invasive procedure based on the PAS principle (one for

light delivery, one for ultrasound detection, and one for the laser-generated ultrasound) [47]. Figure 2-1c recaps that miniaturized PA endoscopy devices are focused on directing the light onto the ultrasound detection region with additional structures such as rotating mirrors [50] or flexible shafts [51]. Intravascular PA imaging devices are typically compact devices; however, they need quite small UTX structures close to the target [61-65] illustrated in Figure 2-1d. This installation of the imaging device creates undesired PA responses (e.g., interference signals, reverberations from excitation signals). Those devices should efficiently reflect different characteristics on plaque types while detecting PA responses in the intravascular region, which suffers from differentiating PA signals even with low frequency bandwidths [53].

In current PAS probe designs, interference signals block/deteriorate the PA signals due to UTXs placed near the target. The received PA signals cannot be distinguished within a very short period of time so that further data processing might be challenging. For example, when the pulsed laser fires, the strong electrical pulse generated by the driver circuit could be easily coupled into the transducer-amplifier loop [66]. In addition, after reflection and backscattering, part of the incident light could directly illuminate the optically absorbing transducer surface and induce a large PA response directly on the transducer. To eliminate the effects of the aforementioned interference signals at the received PA signals, a supplementary component would be added to the probe design.

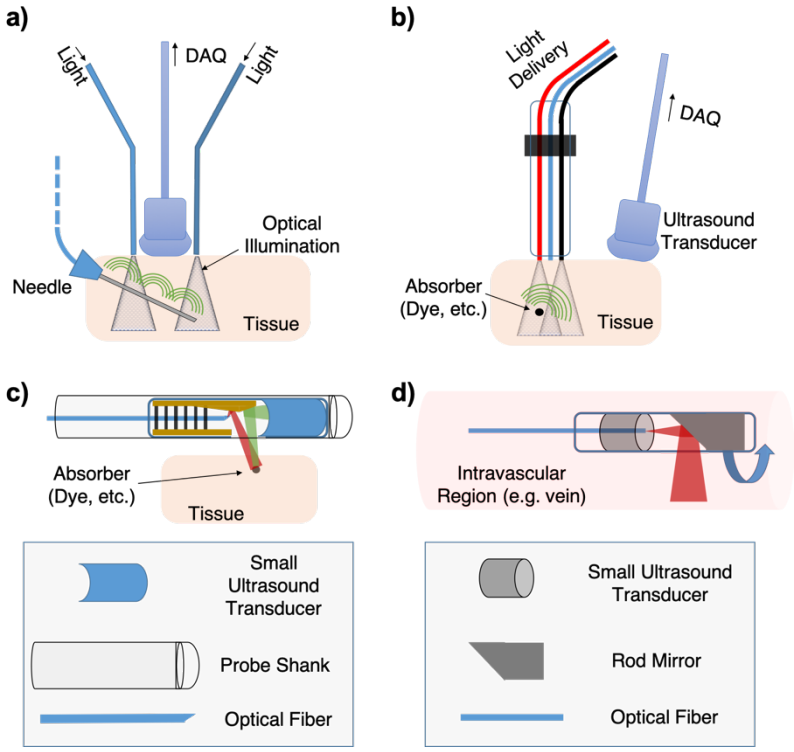

Figure 2-1 Conventional PAS Probe Structures: a) Needle-based Devices (e.g., Guided Biopsy Needles), b) Contact-based PAS Probes, c) PA Endoscopy Probes, and d) Intravascular PA Probes.

2.4. Acoustic Delay Lines (ADLs)

ADLs are acoustic waveguides that transmit ultrasound/PA pulses through itself. A delay line simply adds a specified amount of acoustic time delay. Several materials, liquid mercury [67], solid quartz crystals [68], metallic wires [69], optical fibers [48, 70, 71], and silicon [72, 73] have been used to build ADLs. As an acoustic waveguide, the material should allow high efficiency for acoustic detection and controlling the acoustic time delay. Thus, some materials would be more substantial than others. For example, optical fibers have been effectively used as ADL because of their ready availability [74].

Related to the acoustic velocity of the fused-silica [71, 75], the acoustic time delays for an optical fiber ADL can be controlled from several microseconds to milliseconds by changing the length of the optical fiber. Optical fibers with small diameters allow efficient single-mode acoustic transmission of non-dispersive longitudinal signals (when the diameter is much smaller than the wavelength) [71]. However, low acoustic velocity and high acoustic attenuation (compared to silicon) create modest detection frequency (a few MHz) and explicitly low depth resolution.

As an alternative to the optical fiber ADL (made of fused silica), single-crystalline silicon has higher acoustic velocity and lowers acoustic attenuation in the MHz range [76]. If the cross-section dimension is kept much smaller than the wavelength ($d/\lambda \ll 1$), higher-order longitudinal modes of propagation and mode dispersion would be suppressed [73, 77, 78]. In other words, the dispersion of generated PA (or ultrasound) waves can be kept minimal resulting in good acoustic transmission.

For a 2-inch or 4-inch wafers, tens or even hundreds of ADL can be constructed. Further, it is typically one of the most convenient materials for micromachining because it is a mechanically strong material [72]. After micromachining, it can be assembled into different forms. As an example, it is used for making acoustic multiplexer within microfluidic channels for an ADL application [79]. With the addition of robust holder/linker designs [66, 80], mechanically-stable SADLs with a long time delay can be obtained without sacrificing their acoustic performance.

Geometric parameters of an ADL determine most of the acoustic properties of the ADL. The acoustic time delay changes with the propagation length of the ADL. The PA

amplitude can be increased with a larger contact area, namely the cross-section of the contact end of the ADL to UTX when the material properties remain the same. In addition, the radius of curvature for a coil-shaped (or U-turn) ADL design lowers the PA amplitude due to existing mode conversion in bending portions [72]. Also, the detection frequency and bandwidth of the transmitted signal through the ADL are inversely related to the cross-section dimensions (width & thickness), which affects the axial resolution for the target.

3. PHOTOACOUSTIC SENSING PROBE USING OPTICAL FIBER ACOUSTIC DELAY LINE*

In this section, a new PAS probe design using two optical fibers is presented. Specifically, one optical fiber serves as the optical waveguide for delivering excitation laser pulses onto the target. The second optical fiber functions as an ADL to detect and transmit the generated PA signal from the target to an outside UTX, while creating a desirable amount of acoustic time delay. With the added acoustic time delay, the PA signal will arrive at the transducer after the interference signals diminish and therefore can be easily distinguished in the time domain. Due to its high optical transparency, the direct PA response at the tip of the acoustic delay fiber (ADF) can be minimized. As a result, a clean PA signal originating from the target can be obtained. Furthermore, with the transducer located outside, the PA probe consists of only two optical fibers placed closely to each other. A small probe diameter can be achieved to minimize its invasiveness for *in-vivo* use. For demonstration, a prototype probe was designed, fabricated, and tested with different concentrations of dye solutions and in the biological tissues such as chicken breast tissues with bovine blood. The testing results show that the PAS probe can provide good sensitivity and maintain high linearity over a wide range of dye concentrations. The detection of bovine blood embedded into chicken breast tissue was also conducted to validate its potential usefulness for *in-vivo* PAS applications.

3.1. Experimental Procedure

3.1.1. Probe Design and Construction

Figure 3-1a shows the schematic design of the PAS probe. Two optical fibers are laid side by side along the probe shank. The optical excitation fiber is used to send excitation laser pulses to the target. The ADF is used to receive and transmit the generated PA signal from the target to the UTX with a certain time delay, which is determined by the length and the sound velocity of the ADF. The acoustic delay should be made longer than the duration of the electrical pulse during excitation, such that the real PA signal from the target can be completely distinguished. Both the optical excitation fiber and the ADF are made of fused silica multimode fibers (FT400UMT, THORLABS, Newton, NJ) with a core diameter of 400 μm, a clad layer of 12.5 μm, and an overall diameter of 730 μm. The 400-μm core diameter allows the transmission of μJ ~ mJ laser pulses without damaging the fiber tip. To reduce the acoustic attenuation, the polymer jacket layer of the ADF was removed. The fiber core together with the cladding layer was placed inside a polyimide tubing (Microlumen, Oldsmar, FL) with an inner diameter slightly larger than that of the ADF. The polyimide tubing provides good structural protection and also acoustic insulation for the ADF. With a snug fitting, it does not cause extra acoustic attenuation for the PA signal transmission.

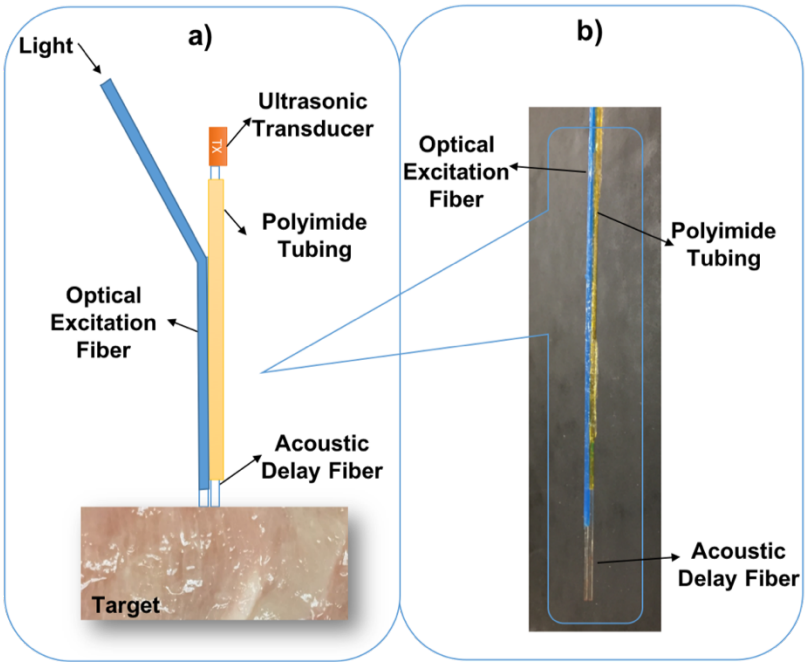

Figure 3-1 a) Schematic of PAS Probe Design and b) Picture of the Probe Shank with Glued Optical Excitation Fiber and ADF.

During the operation of the probe, the ADF can easily contact with surrounding tissue or media. Without acoustic isolation, the transmitted PA signals can be easily damped out. With the use of a polyimide tubing to encapsulate the ADF, the optical delivery fiber and the ADF can be directly glued together without affecting the performance (Figure 3-1b). In this way, the PAS probe can be very compact, easy to build, and therefore suitable for *in-vivo* use. In addition, the optical excitation and acoustic detection areas can be largely overlapped to provide an optimal sensing condition.

The ADF is interfaced with a homemade piezoelectric (PZT) (APC 851, APC International, Ltd., Mackeyville, PA) transducer with a thickness of 1.1 mm. For robust interfacing contact between the ADF and the transducer, an acrylic spacer and a holder

are used. Acrylic spacers and holders were cut from a 1.5 mm-thick acrylic sheet with a laser cutter (Universal Laser Systems, PLS6.75). The resonance frequency of the PZT transducer's thickness mode is ~1.85 MHz. The size of the transducer (4.0 x 2.0 mm^2) is kept as small as possible to reduce the parasitic capacitance to the transducer. Since both PZT and silica have high acoustic impedance, no matching layer was applied between them. A thin layer of epoxy was applied to directly bond the transducer onto the tip of the fiber. The transducer frequency is chosen based on the non-dispersive single-mode transmission frequency limit of the optical fiber, which is usually around 0.1~0.2 c/d, where c and d are the acoustic velocity and diameter of the fiber core, respectively [69, 70]. Suppose the acoustic velocity is 5500 m/sec and the fiber core diameter is 400 μm, this gives 1.25~2.5 MHz as the acoustic transmission frequency achieved from the ADF. Distortion will occur for ultrasound transmission at frequencies much higher than this value due to dispersion and excitation of multiple modes. To increase the acoustic detection frequency range, the single large-core ADF could be replaced with a bundle of optical fibers with a smaller core diameter. However, because the ultrasound transmission along the optical fibers is very sensitive to the surface and contact conditions, careful measures have to be taken to ensure good acoustic isolation for every fiber in the bundle, which otherwise would be difficult to be implemented in practice.

3.1.2. Ultrasound Transmission of Acoustic Delay Fiber

To identify optimal acoustic transmission conditions for the PA signals, two-port ultrasound testing is conducted to study the ultrasound transmission in the ADF under three conditions: 1) with the jacket layer, 2) with the jacket layer removed, and 3) placed

in polyimide tubing after the jacket layer removed. To determine the actual acoustic velocity and attenuation of the ADF (without jacket layer and tubing), six fiber samples with different lengths ranging from 8.4 cm to 54 cm are also prepared.

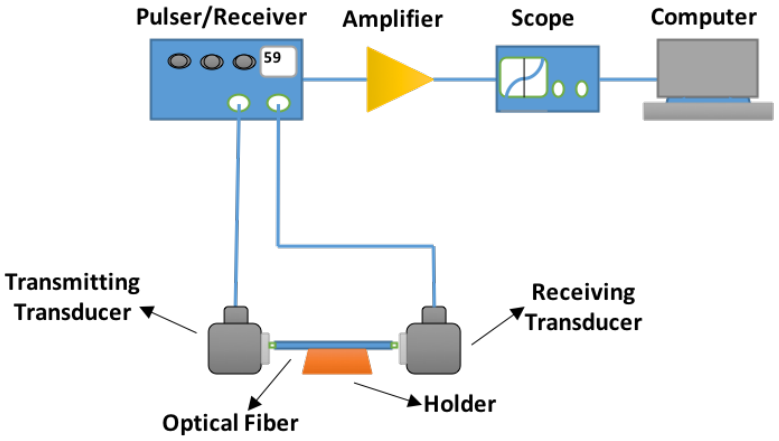

Figure 3-2 A Two-Port Ultrasound Testing Setup for the ADF.

Two 2.25 MHz flat contact transducers (V104 and V125, Olympus NDT, Waltham, MA, USA) are used to transmit and receive the ultrasound signals (Figure 3-2). The two ends of the ADF are polished and contacted onto the transmitting and receiving transducers, respectively. Mineral oil is applied onto the contacts between the ends of ADF and the surfaces of transmitting & receiving transducers to enhance coupling efficiency and minimize unwanted reverberation. The pulser/receiver (5072PR, Olympus NDT, Waltham, MA) is set to the transmission mode, which sends a driving voltage pulse to the transmitting transducer to generate ultrasound signals and also amplified signals detected by a receiving transducer. Each received ultrasound signal is

averaged 16 times and recorded on a digital oscilloscope (TDS2002C, Tektronix Inc., Beaverton, OR, USA) to determine their peak amplitude and time delay.

3.1.3. Verification of Interference Signal Separation

The time delay separating the received PA signals and interference signals is verified with a piece of black tape as the target. The black tape is a good optical absorber, which can generate strong PA signals. In addition, a highly-reflectively mirror surface is also used as the target to test the PA response of the tip of the ADF, which should be minimized as it will mix with the real PA signal from the sensing target. With a high reflectivity, the mirror surface itself is a weak PA generator. It reflects much of the incident light back onto the ADF, which provides a good scenario for observing the PA response at its tip.

3.1.4. Dye Characterization

Figure 3-3 shows the test setup of the dye characterization experiment. This setup is also used for the verification of interference signal separation (except that a black tape and a mirror are used as the targets). The dye concentration testing is a common procedure to evaluate the sensitivity and linearity of a PA sensing or imaging system. When a single dye is used, the absorbed optical energy and the resulting PA response (i.e., the first peak of the PA signal from the transducer) should increase linearly with the dye concentration. By measuring the PA signals from dye solutions with different concentrations, the linearity of the PAS probe can be characterized. In addition, the lowest detectable dye concentration can serve as a good indication of the sensitivity.

The excitation light pulse is delivered from a 532 nm Q-switched Nd:YAG laser (SPOT-10-200-532, Elforlight Ltd, Northants, UK) with a 1.75 ns pulse width and a 1 kHz pulse repetition rate. The output of laser energy is 20 μJ/pulse. The output laser beam was focused down to ~0.7 mm in diameter and incident onto the input end of the optical excitation fiber. Since the core diameter of the optical excitation fiber (~400 μm) is smaller than the focused beam diameter, only part of the incident light is coupled. The pulse energy measured at the output end of the optical excitation fiber was ~1.31 μJ/pulse. Based on the core diameter of the optical excitation fiber, the maximal optical fluence at the output end the of the optical excitation fiber is estimated to be 1.04 mJ/cm^2, which is well below the ANSI safety limits for biological tissues of 20 mJ/cm^2 [32]. The generated PA signals are detected and delayed by the ADF and serially received by the built-in single-element PZT transducer. The received PA signals are amplified with a homemade printed circuit

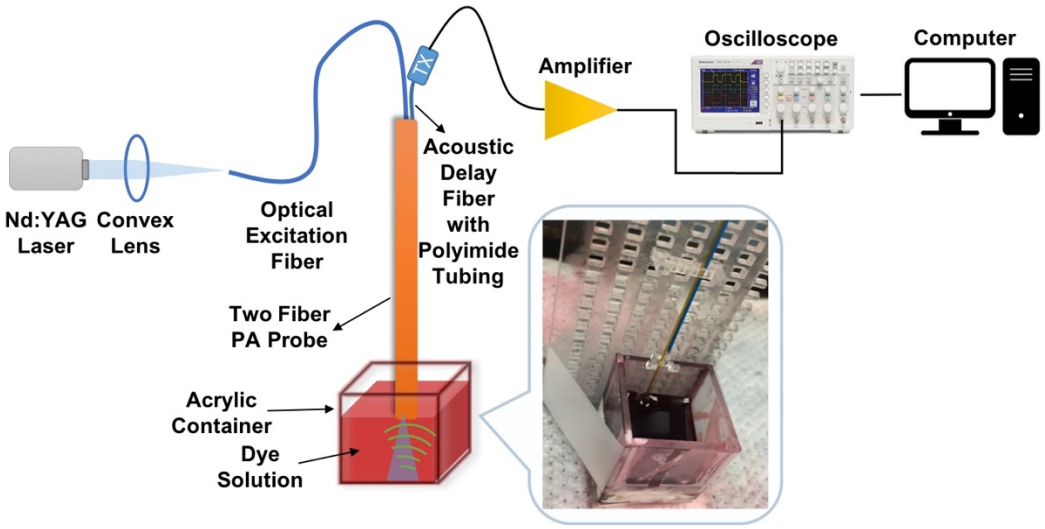

Figure 3-3 Schematic of Dye Testing Setup.

board (PCB) pre-amplifier with a gain of 40 dB. The amplified PA signals are displayed on the oscilloscope and stored on the computer.

To prepare the dye solutions as the sensing target, black and red dye powders (Rit® Dye, Phoenix Brands, Stamford, CT) are dissolved in DI water with an initial concentration of 0.1 g/mL or 10% (wt/vol %). The stock solution is further diluted to lower concentrations by adding suitable amount of water. The dye solution to be measured is transferred into an acrylic container. The PAS probe is first mounted onto a Z-stage and gradually lowered till the ends of both the optical excitation fiber and the ADF just touched the surface of the dye solution (Figure 3-3). For each concentration, The PA measurement is repeated five times. The captured PA voltages are averaged to determine the overall PA response.

3.1.5. Detection of Bovine Blood in Chicken Breast

To demonstrate its potential usefulness for *in-vivo* sensing in biological tissues, the PAS probe is used to detect bovine blood (Quad Five, Ryegate, MT, USA) embedded inside a chicken breast tissue. The bovine blood is injected into a small plastic pouch made of clear food wrap film and placed inside a piece of chicken breast tissue. The tip of the PAS probe is contacted onto the chicken breast tissue (see Figure 3-9 for its diagram). The thickness of the chicken breast tissue separating the blood pouch and the probe tip is varied between 0 mm and 3 mm. Under the same testing conditions for dye characterization, the PA measurement is repeated six times. The captured PA voltages are averaged to determine the overall PA response in the bovine blood detection test.

3.2. Results and Discussion

3.2.1. Ultrasound Transmission of Acoustic Delay Fiber

Figure 3-4a shows the received ultrasound signal after traveling through the ADF (with the jacket layer) with a length of 100 mm. The ultrasound signal arrived at the receiving transducer with a time delay of ~18.4 µs while the source signal can be seen at the zero point in the time domain. However, with the plastic jacket layer, the acoustic attenuation is high. For comparison, the ultrasound transmission testing is repeated after the jacket layer was removed and also after the optical fiber is placed inside the polyimide tubing. As shown in Figure 3-4b, the acoustic attenuation is significantly reduced after the removal of the jacket layer. A similar result is obtained after the optical fiber (without the

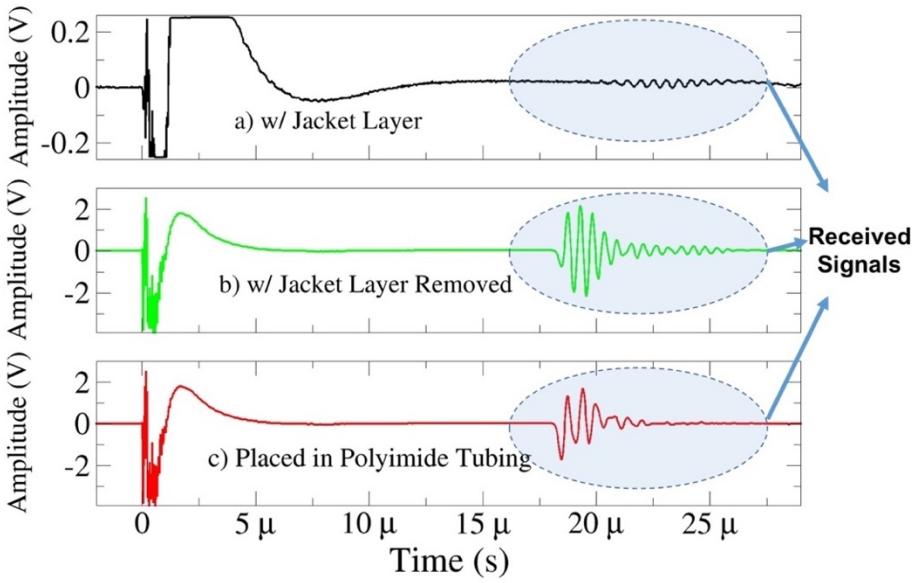

Figure 3-4 Received Ultrasound Signals after Travelling through the ADF for Different Fiber Conditions: a) with the Jacket Layer, b) with the Jacket Layer Removed, and c) Placed in Polyimide Tubing (with the Jacket Layer Removed).

jacket layer) was placed inside the polyimide tubing (Figure 3-4c), which shows that the polyimide tubing does not significantly affect the ultrasound transmission through the ADF.

The acoustic delay time increases almost linearly with the length of the fiber. Figure 3-5a represents the linear relationship between the acoustic time delay and the length of the fiber. An average acoustic velocity of the fiber is determined to be ~5434 m/s, which is close to the typical sound velocity of fused silica [70, 71]. Figure 3-5b shows the peak-to-peak voltage amplitude of the received ultrasound signals through the tested fibers. Using the peak-to-peak voltage amplitude of the shortest fiber as the reference, the acoustic loss of each fiber is calculated as $20*\log(Vout_a / Vout_b)$, where "$Vout_a$" refers to the peak-to-peak voltage amplitude of that fiber and "$Vout_b$" refers to that of the shortest fiber. The acoustic attenuation (per unit length) of each fiber is determined by dividing the acoustic loss by the length difference (Δl) between the two fibers. Due to the possible

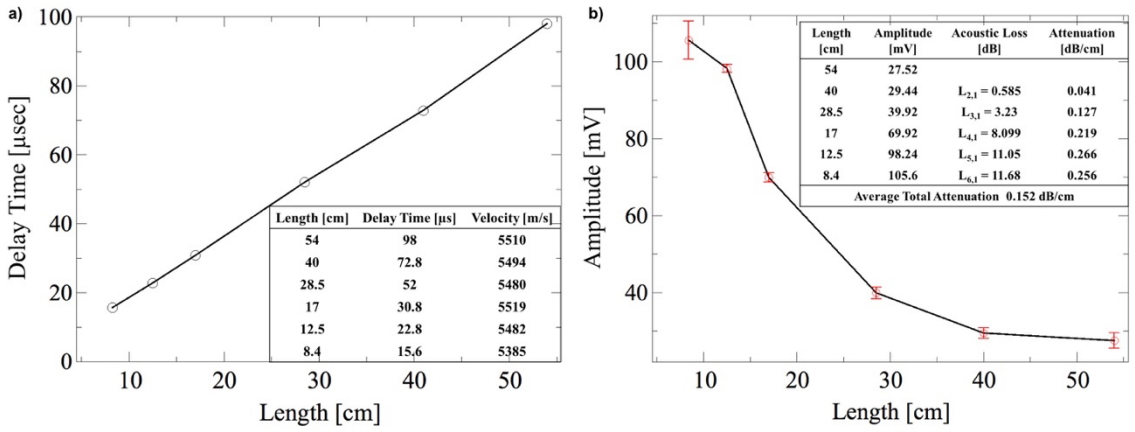

Figure 3-5 Two Port Ultrasound Test Through Optical Fibers with Different Lengths for a) Acoustic Time Delay, Velocity and b) Acoustic Loss, Attenuation.

different fiber/transducer contact conditions during the testing, the acoustic attenuation (@ 2.25MHz) of the fiber ranges from 0.041 to 0.266 dB/cm (due to different contact conditions in each measurement) with an average value of 0.152 dB/cm.

Although the ultrasound transmission testing is able to reveal the attenuation in the ADFs, the potential PA signal reduction caused by the use of the ADF between the target and transducer (compared with direct target-transducer contact) also needs to be studied. In the experimental setup, a direct contacting transducer onto the target will completely block the excitation light, which makes the reflection-mode testing not feasible. Therefore, transmission-mode testing was performed on a black tape target to compare the difference in the PA detection performance with and without the acoustic delay fiber. As shown in Figure 3-6, the peak-to-peak PA voltage without the ADF is around 16.2 mV. The peak-to-peak PA voltage with the ADF is around 8.2 mV, which is due to a smaller contact area

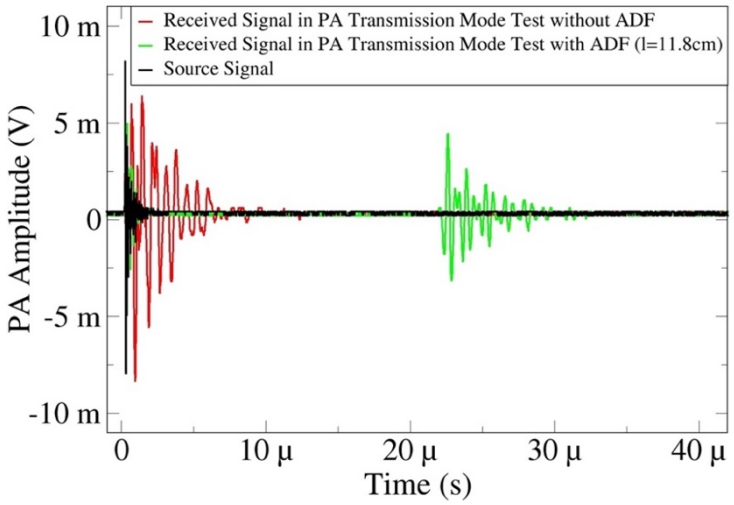

Figure 3-6 Received PA Signals in Transmission Mode with and without ADF.

and also, the acoustic attenuation in the ADF. With a delay length of 11.8 cm, the difference in the arrival time between the two PA signals is around 21.60 μs, which approximately matches with its delay time and typical sound velocity of fused silica.

3.2.2. Verification of Interference Signal Separation

Figure 3-7 shows the comparison of received signals when a piece of black tape and a highly reflective mirror surface was used as the target. The data acquisition (DAQ) is triggered by the firing of the pulsed laser. The PA signal from the black tape target arrived at the transducer after a delay of ~18 μs, which matches with the delay time determined in the ultrasound transmission testing of ADF. Although the strong signal still exists at the moment of the firing of the pulse laser, there is no noticeable PA signal with using a mirror as the target. This shows that the PA response of the tip of the ADF is negligible, which can be explained by its high optical transparency and low absorption from the mirror.

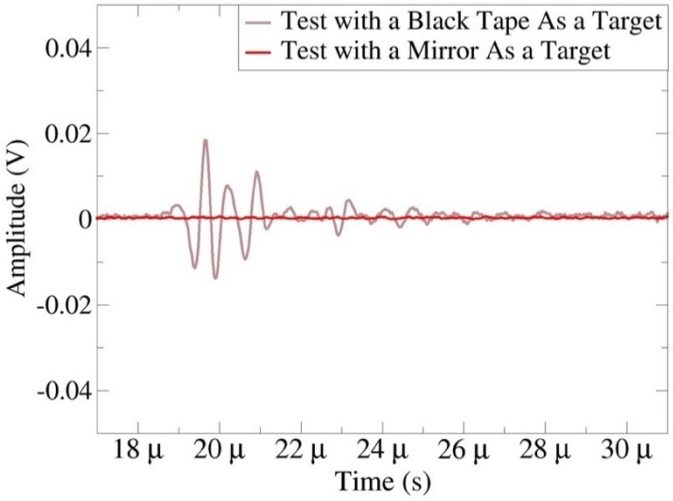

Figure 3-7 The Received PA Signal after Travelling through the ADF from The Black Tape and Mirror as the Target.

3.2.3. Dye Characterization and Bovine Blood Detection

Figure 3-8a shows representative PA signals received from a 0.04 g/mL red dye solution and a 0.04 g/mL black dye solution. The change in the average PA voltage amplitude of the first peaks as a function of the black dye concentration is shown in Figure 3-8b. The peak-to-peak PA voltage increases almost linearly with the dye concentration with a significant correlation ($R^2 = 0.98291$ for black dye and $R^2 = 0.88371$ for red dye). When the black dye concentration is reduced down from 0.1 g/mL to 0.002 g/mL, the signal-to-noise ratio (SNR) dropped from 20.6 dB to 2.67 dB, the received PA waveform starts to bury under the noise level. This indicates a detection limit of about 0.002 g/mL. When the red dye concentration is reduced down from 0.1 g/mL to 0.005 g/mL, the SNR dropped from 24.7 dB to 3.37 dB. This indicates a detection limit of about 0.005 g/mL for red dye solution in the PA experiment.

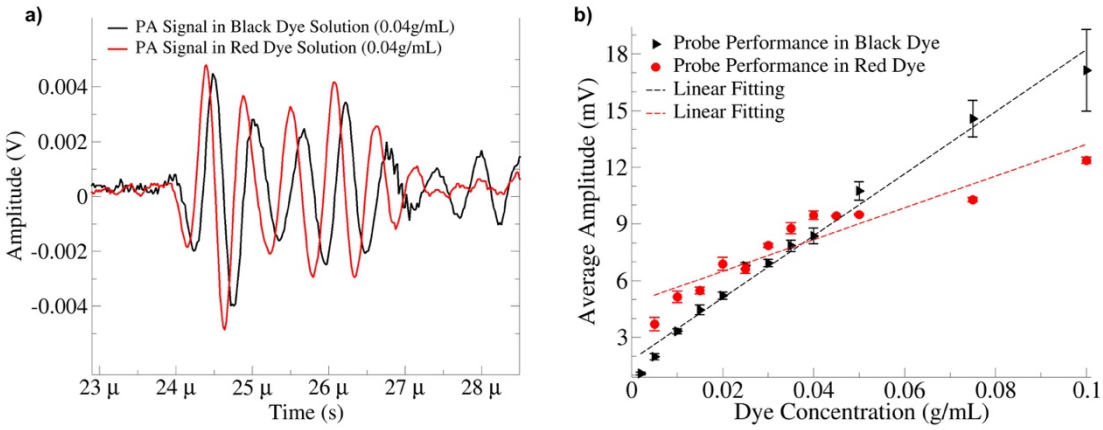

Figure 3-8 PA Testing Results of Black and Red Dye Solutions a) PA signals from Black and Red Dye Solutions of 0.04g/mL Concentration and b) Average Amplitudes of PA signals from Black and Red Dye Solutions with Different Concentrations.

Figure 3-9 shows the test setup and recorded PA signals from the bovine blood depending on the thickness of the chicken breast tissue. The PA signal amplitude drops when the thickness of the chicken breast increases. The total time delay of the PA signal is determined by the arrival time of the PA signal. The time delay in the chicken breast tissue between the probe tip and the blood is calculated by subtracting the time delay of the ADF (~21.83 µs) from the total time delay (~23.87 µs with 3 mm thick chicken breast piece). Assuming the acoustic velocity of the chicken breast is ~1540 m/s, the distance between the probe tip and the bovine blood is estimated based on the calculated time delay in the chicken breast tissue, which matches with the actual thickness of the breast tissue. First positive peaks also provide good comparisons for different thicknesses of the chicken breast tissue. This test shows that the PAS probe can detect not only the existence of the blood target but also determine its distance based on the acoustic travel time.

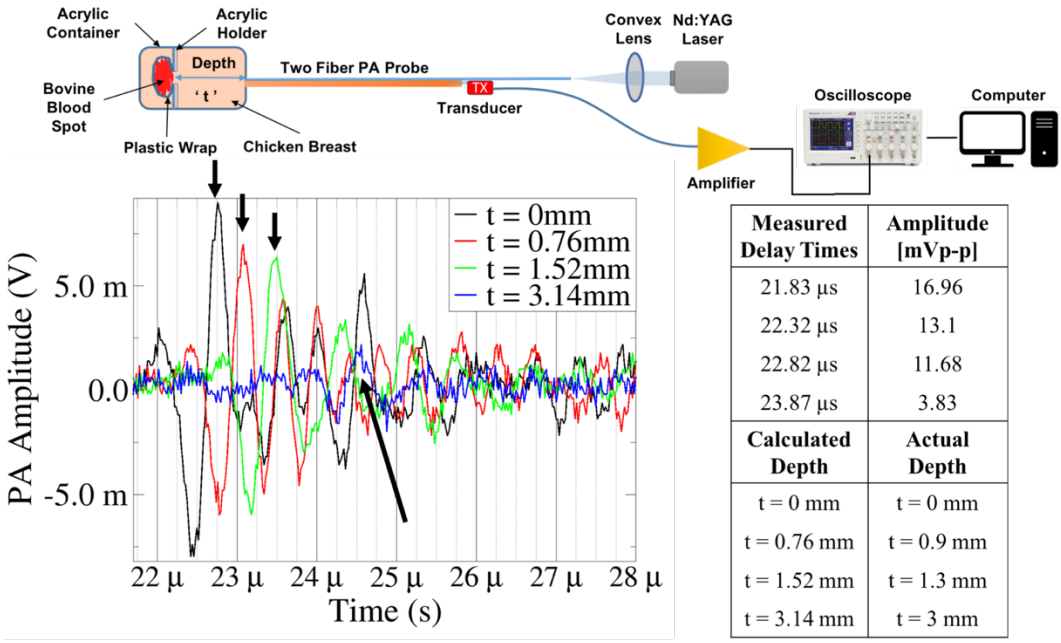

Measured Delay Times	Amplitude [mVp-p]
21.83 µs	16.96
22.32 µs	13.1
22.82 µs	11.68
23.87 µs	3.83
Calculated Depth	**Actual Depth**
t = 0 mm	t = 0 mm
t = 0.76 mm	t = 0.9 mm
t = 1.52 mm	t = 1.3 mm
t = 3.14 mm	t = 3 mm

Figure 3-9 Detection of Bovine Blood in Chicken Breast Tissue.

4. PHOTOACOUSTIC SENSING PROBE USING SINGLE OPTICAL FIBER ACOUSTIC DELAY LINE[†]

In this section, a new PAS probe design using a single optical fiber for both light delivery and ultrasound detection is presented. This is made possible by the development and use of an optically transparent UTX, which allows the excitation light to pass through and travel along the optical fiber to reach the target. In return, the transducer senses the generated PA signal transmitted through the optical fiber as an ADL. To make the optically transparent UTX, single-crystalline piezoelectric substrates, and suitable electrode materials have been investigated. For demonstration, a prototype probe was designed, fabricated, and tested with different concentrations of dye solutions and biological tissues with an embedded target. Compared with the two-fiber PAS probe design, the single-fiber design can provide an even more compact probe structure. In addition, the light delivery and the ultrasound detection areas are completely overlapped with each other, resulting in an ideal configuration for PA signal detection.

4.1. Probe Design and Construction

Figure 4-1a shows the schematic design of the PAS probe. It consists of one single optical fiber laid out along the probe, which is housed inside a polyimide tubing. The polyimide tubing provides good structural protection and also acoustic insulation for the optical fiber [81, 82]. The optical fiber serves as a combined optical waveguide and an

[†] Reprinted with permission from "A Photoacoustic Sensing Probe Using Single Optical Fiber Acoustic Delay Line" by Ustun A. K. and Zou J., IEEE Sensors Journal, 19, 19, pp. 8714-8719, [89] © 2019 by IEEE

ADL for sending laser pulses to the target and transmitting PA signal back from the target. To achieve this, the transducer is made optically transparent to avoid blocking the excitation light. A hollow needle can be used to provide better stability for the fiber tip of the probe. Figure 4-1a also shows the constructed prototype of the single optical fiber PA probe, which was securely positioned in a few acrylic spacers for stable measurements. Through the single optical fiber, the path of the optical signal and in return, the path of the generated PA signal are identical (Figure 4-1b).

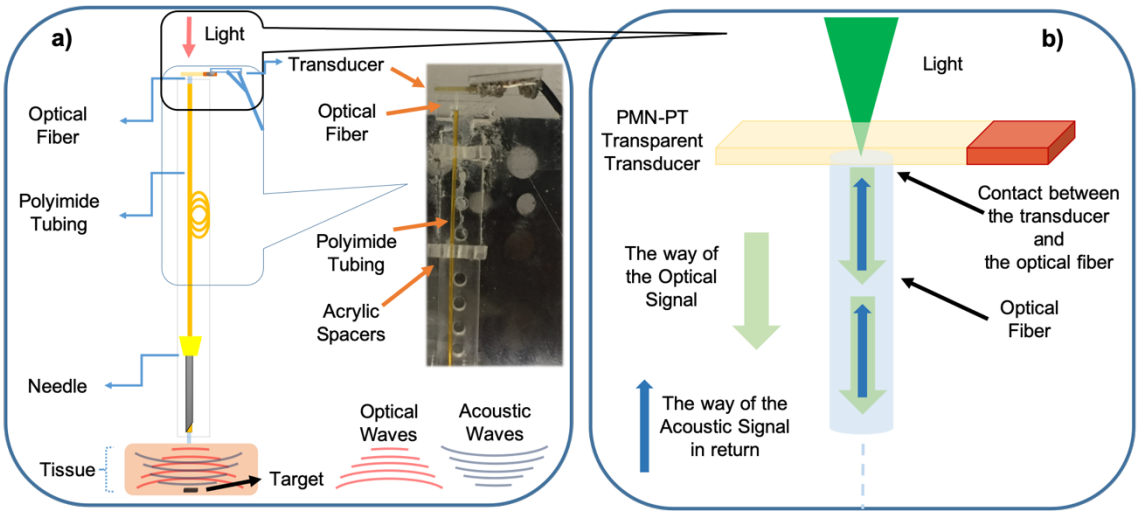

Figure 4-1 a) Schematic of PAS Probe Design & Picture of the Constructed Prototype and b) Working Principle of the Single Fiber PA Probe.

4.1.1. Optical Fiber Acoustic Delay Line

A single multimode optical fiber (FT400UMT, 0.39NA, Thorlabs, Newton, NJ) is used to make the optical fiber acoustic delay line. The polymer jacket layer of the ADF was removed to reduce the acoustic attenuation. The fiber core together with the cladding

layer (12.5-μm thick) was placed inside a polyimide tubing (Microlumen, Oldsmar, FL) with an inner diameter (0.53 mm) slightly larger than that of the ADF. The polyimide tubing provides good structural protection and also acoustic insulation for the ADF. Without this isolation, the transmitted photoacoustic signals can be easily damped out by surrounding media. The diameter of the polyimide tubing does not significantly affect the PA response, as long as the optical fiber is loosely fitted inside the tubing. Therefore, a polyimide tube with an inner diameter slightly larger than the outer diameter of the optical fiber was used.

With a core diameter of 400 μm, the multimode optical fiber provides a good balance of both optical and acoustic performances [74]. First, it can transmit tens of μJ level nanosecond laser pulses without burning the tips. Second, the non-dispersive single-mode transmission frequency limit of the optical fiber is around 0.1~0.2 c/d, where c and d are the acoustic velocity and the core diameter, respectively [71]. Suppose the acoustic velocity of the fiber core is ~5500 m/sec, this gives 1.25~2.5 MHz for a core diameter of 400 μm. At 1~2 MHz, the acoustic attenuation of the 400-μm fused silica core is very low, especially after the jacket layer is removed [81, 82]. Therefore, the length of the optical fiber (and also the probe) can be determined mainly based on the need of the actual applications, as long as it is long enough to provide sufficient acoustic time delay to separate the real PA signal from interference caused by the firing of the pulsed laser.

A two-port ultrasound transmission test is performed to characterize the acoustic properties of the optical fiber (with jacket layer removed and placed inside the polyimide tubing). Two 2.25 MHz flat contact transducers are used to transmit and receive the

ultrasound signals (Figure 4-2a). The two ends of the ADF were polished and contacted onto the transmitting and receiving transducers, respectively. Mineral oil was applied onto the contacts between the ends of the optical fiber and the surfaces of transmitting & receiving transducers to enhance coupling efficiency and minimize unwanted reverberation. Each received ultrasound signal is averaged 16 times and recorded on a digital oscilloscope. Figure 4-2b shows the ultrasound transmission of the optical fiber with a length of 54 mm. The received ultrasound signal is located at ~99 μs, which is close to the calculated time delay based on the acoustic velocity of the fused silica [70, 71]. Figure 4-2c shows the frequency spectrum of the transmitted ultrasound signal. The received (time-domain) ultrasound signal is truncated to remove the unwanted reverberations (i.e., the long-tail). In other words, only significant time-domain information of the received ultrasound signal is selected. Fast-Fourier Transform (FFT) was performed in MATLAB® to calculate the frequency spectrum. The central frequency of the received signal is seen at 2 MHz, matching the lowest longitudinal-mode transmission signals through the optical fiber [71].

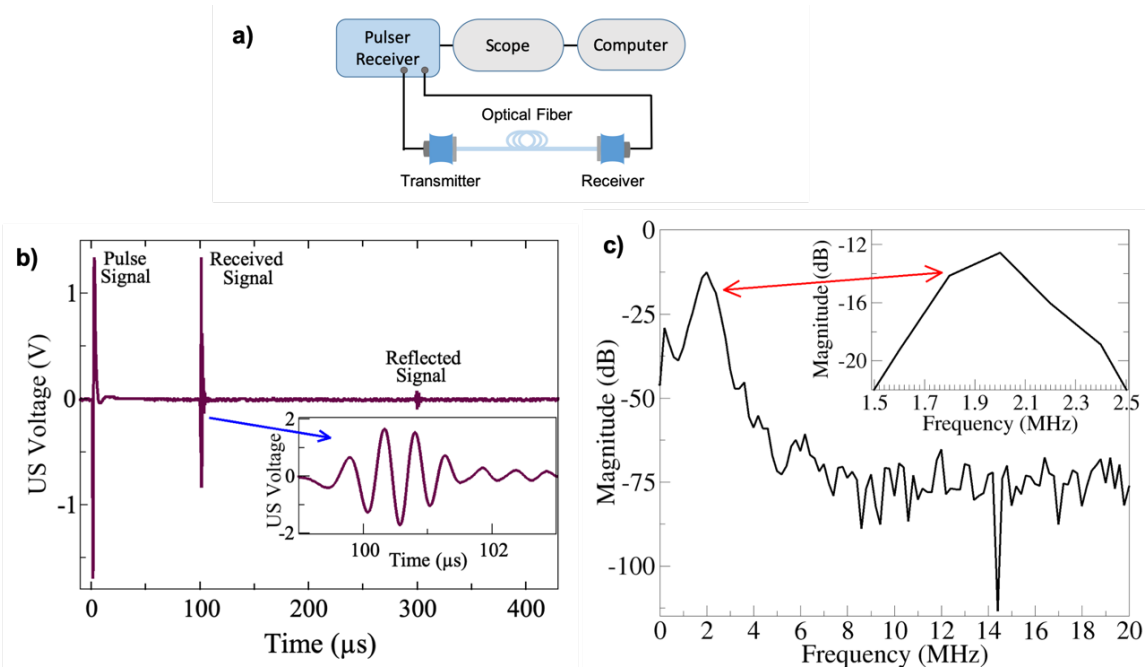

Figure 4-2 Two Port Ultrasound Transmission Test Results for the Optical Fiber Acoustic Delay Line with no Jacket Layer a) Testing Setup b) Pulse, Received and Reflected Signals c) Frequency Spectrum of the Received Signal through the Optical Fiber Acoustic Delay Line.

4.1.2. Transparent Transducer

A piece of single-crystalline PMN-PT ($Pb(Mg_{1/3}Nb_{2/3})$–$PbTiO_3$) substrate (HC Materials Corporation, Bolingbrook, Illinois, USA) is used to make the transparent transducer due to its good optical transparency and piezoelectric property. It has 27-33% "PT" content that varies the piezoelectric constant from 2000 pC/N and 3000 pC/N with <001> poling [83, 84]. The thickness of the PMN-PT substrate is 0.6 mm, which provides a resonance frequency of ~3.5 MHz in the thickness mode [83], which is high enough to cover the center frequency of the optical fiber (2 MHz) and its effective bandwidth. The surface area (~ 5 mm x 2 mm) of the PMN-PT transducer is kept small to reduce the

parasitic capacitance to the transducer. No matching layer is added between the PMN-PT transducer and the optical fiber because their acoustic impedance is close to each other. Both top and bottom surfaces of the PMN-PT substrate are first polished to reduce the surface roughness. To form the transparent electrodes, a 120-nm thick indium-tin-oxide (ITO) layer is coated on both surfaces by sputtering which provides both sufficient optical transparency and good electrical conductivity [47]. To facilitate the wiring, two chromium and copper contact pads (one on the top and one on the bottom) are directly formed by evaporation through a shadow mask. After the deposition is complete, the PMN-PT transducer is mounted onto a glass holder. For the connection between the transducer and the glass pad, silver epoxy (Von Roll 3022 E-Solder®, Conductive Adhesive, Schenectady, NY, USA) is applied and cured. Transducer mounting is completed by attaching an SMA connector to the glass-transducer assembly (Figure 4-3).

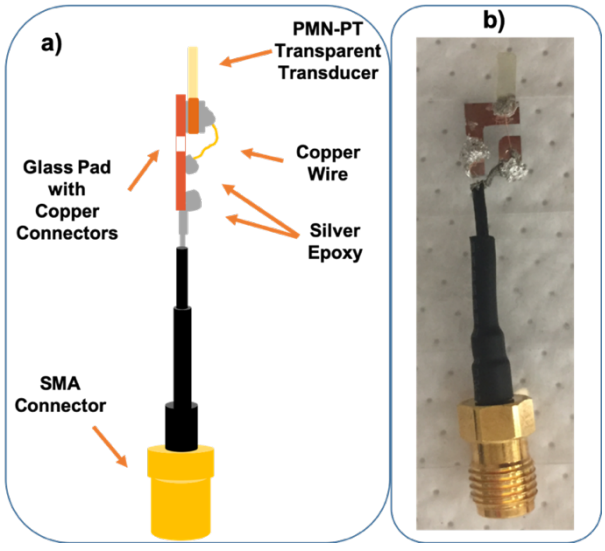

Figure 4-3 Optically Transparent PMN-PT Transducer Assembly in a) Side View Illustration and b) Photo of the Assembly.

4.2. Testing and Characterization

4.2.1. PA Testing Setup

The testing setup of the PAS probe is shown in Figure 4-4. The light source is an Nd:YAG laser (SPOT-10-200-532, Elforlight Ltd, Northants, UK) operating at the wavelength of 532 nm. Its pulse duration and maximum output energy are 1.75 ns and 20 μJ/pulse, respectively. The pulse repetition rate is set to 1 kHz. The output beam diameter was roughly 0.7 mm. A convex lens is used to focus the light onto the transparent transducer at a specific point. The optical fiber is aligned to the focal point of the light to provide maximal coupling efficiency. Multiple acrylic spacers and polyimide tubing are used to fix the optical fiber in a stable position. The focused light transmitted through the transparent transducer and the optical fiber, and then reached the target, which is made of a black vinyl electrical tape (Scotch® Super 33+ Vinyl Electrical Tape, USA). The black vinyl electrical tape has a high optical absorption coefficient and therefore provides high efficiency for PA signal generation. The contact conditions between the fiber tip and the transducer and target are carefully maintained during tests to reduce acoustic coupling loss between the optical fiber and the target or between the transducer and optical fiber. A homemade printed circuit board (PCB) amplifier is used to amplify the acoustic signal coming from the transparent transducer. Its amplitude gain is set to be 23 dB based on the values of the feedback resistor and input resistor in an inverting amplifier [66]. The amplified PA signal is received by a digital oscilloscope with a sampling rate of 100 MHz.

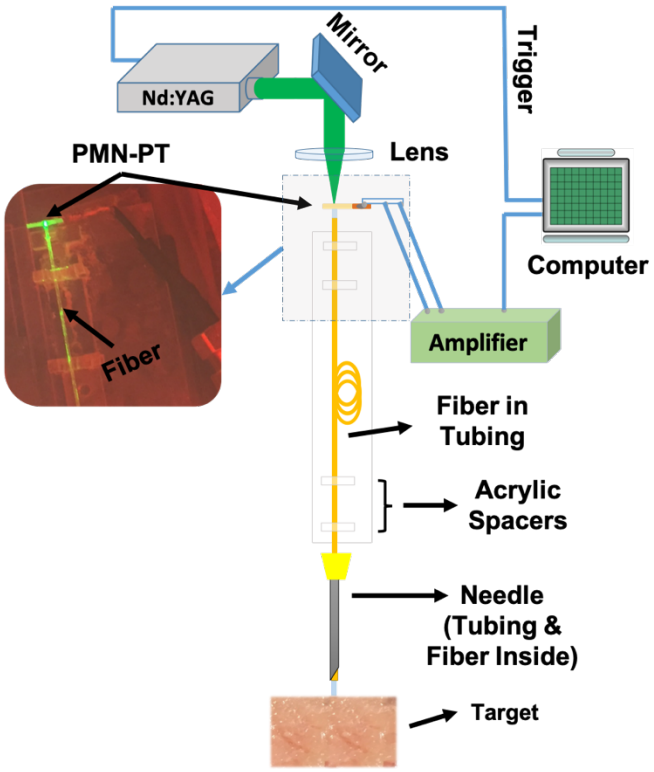

Figure 4-4 PAS Probe Testing Setup.

4.2.2. Probe Characterization

After necessary alignments were made, the overall optical transmission efficiency through the transparent transducer was first characterized. The target is replaced with the photodetector of an optical power meter. As a reference measurement, the transducer was first removed from the measurement setup and the optical power at the end of the fiber was measured by the power meter. The transducer substrate is put back and the optical power was measured again. The output laser power measured at the tip of the PAS probe with and without the transparent transducer is 1.464 mW and 5.88 mW, respectively, which corresponds to an overall optical transmission efficiency of 24.9%. For comparison,

an un-polished and also a thicker PMN-PT substrate is also measured to evaluate the transmission loss due to surface scattering and optical absorption inside PMN-PT (Table 4-1). As listed in Table 4-1, both thickness and surface condition of the PMN-PT substrate play a significant role in the optical transmission efficiency. To avoid excessive attenuation due to absorption, the thickness of the PMN-PT substrate needs to be carefully chosen to satisfy the requirements on both optical and acoustic performances. In addition, the surface roughness should be minimized to reduce the light loss due to scattering. Moreover, both PMN-PT and ITO have excellent transparency in the visible and near-infrared range. Since the optical transparencies of PMN-PT and ITO have been well studied before [85-87], the optical transparency for the transducer is quantified at a single wavelength.

Table 4-1 Optical Transmission Efficiency Measurements for Different Transducer Samples.

Material	Thickness	Transmission Efficiency (%)
Unpolished PMN-PT	1.6 mm	~2 %
Unpolished PMN-PT	0.6 mm	~11 %
Polished PMN-PT with ITO	1.6 mm	~9 %
Polished PMN-PT with ITO	0.6 mm	~25 %

Figure 4-5a shows a representative PA signal received from the black tape target after being averaged by sixteen times. In addition to the original PA signal (which arrived

first), the second, third, and fourth reflected signals were also received at later times. This shows that the optical fiber can serve as a low-loss ADL to transmit the PA signal from the target to the transducer. Figure 4-5b shows the FFT spectrum of the received PA signal. It covers a wide frequency range up to 2.1 MHz, which corresponds to the cut-off frequency of the lowest longitudinal mode of the optical fiber.

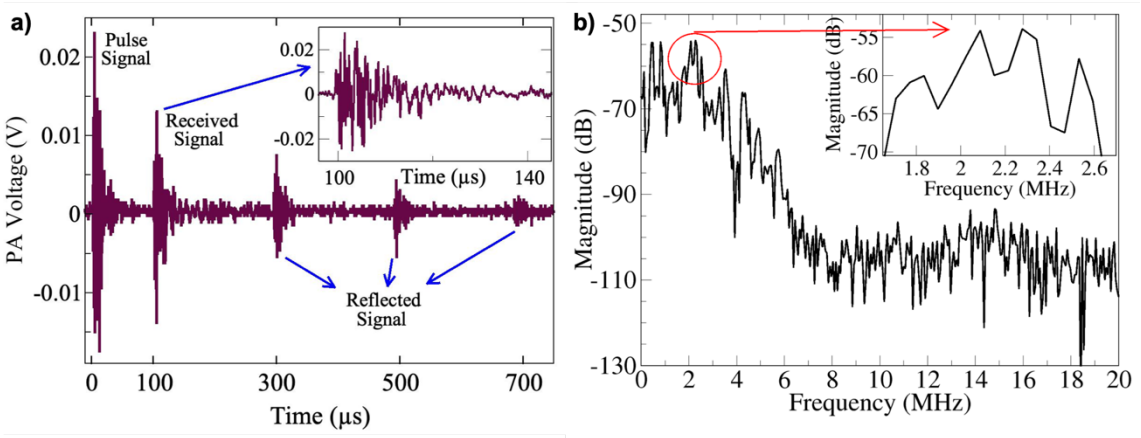

Figure 4-5 PA Test Results of the PAS Probe with Black Tape as the Target a) Pulse, Received, and Reflected Signals b) Frequency Spectrum of the Received PA Signal.

For probe characterization, different laser power levels were used to reveal the relationship between the optical fluence and the resulting PA signal strength (Figure 4-6). The laser pulse energy and the optical fluence are determined based on the measured laser power, the pulse repetition rate, and also the estimated illumination area. At the probe tip, the maximal pulse energy was 5.36 μJ/pulse and the maximal optical fluence is 4.27 mJ/cm^2, which is far below the ANSI (American National Standard Institute) safety limit of 20 mJ/cm^2 [32]. As shown in Figure 3-6, the PA voltage increase with the optical

fluence with a strong linear correlation ($R^2 = 0.991$). With an almost constant noise floor, the SNR increases with optical fluence by following a logarithmic relationship.

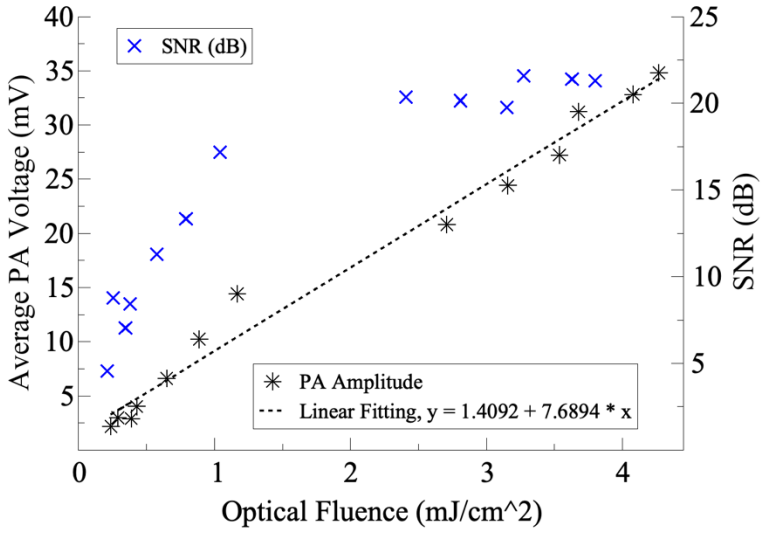

Figure 4-6 PA Voltage and SNR vs. Optical Fluence.

4.2.3. Dye Characterization

The PA testing setup is also used to demonstrate the PA characterization of dye concentration. Dye solutions are prepared with red dye powders (Rit® Dye, Phoenix Brands, Stamford, CT). Powders are first dissolved in DI water and are transferred into an acrylic container. The PAS probe is first mounted onto a Z-stage and gradually lowered till the tip of the optical fiber just touches the surface of the dye solution. For each concentration, the PA measurement is repeated five times. The captured PA voltages are averaged to determine the overall PA response.

Figure 4-7a shows the PA signals received from 0.1 g/mL, 0.04 g/mL, and 0.01 g/mL red dye solutions. The change in the average PA voltage of the first peaks as a function of the red dye concentration from 0.001 g/mL to 0.1 g/mL is shown in Figure 4-7b. The peak PA voltage increases with the dye concentration, showing a significant linear correlation between the dye concentration and the PA response of the probe ($R^2 = 0.928$). When the dye concentration was reduced down from 0.1 g/mL to 0.001 g/mL, SNR dropped from 19.2 dB to 5.63 dB. The received PA waveform started to bury under the noise level, which indicates a detection limit of about 0.001 g/mL.

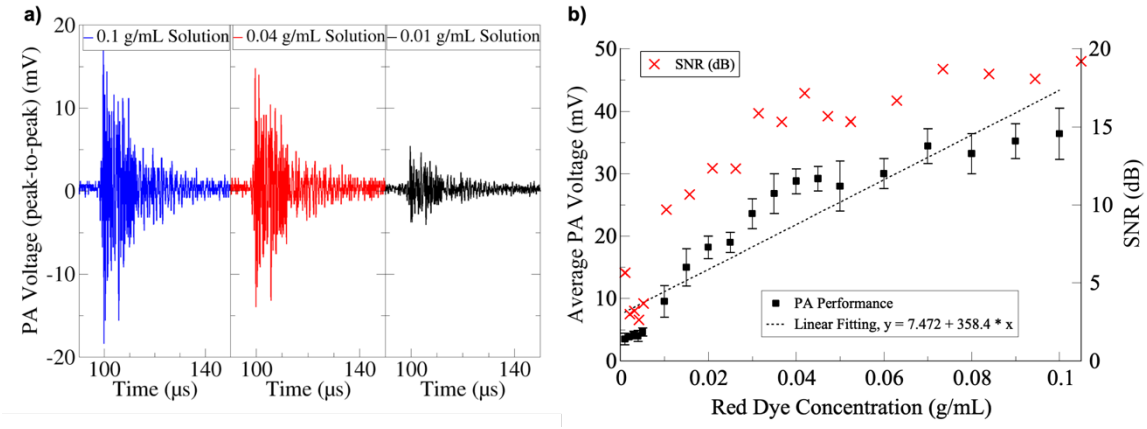

Figure 4-7 a) PA Signals Received from Red Dye Solutions with Different Concentrations: (Left) 0.1 g/mL, (Middle) 0.04 g/mL, and (Right) 0.01 g/mL b) PA Voltage and SNR vs. Dye Concentration.

4.2.4. Target Depth Detection in Biological Tissues

Detecting targets at different depths in biological tissues is another important function of the PAS probe [88]. The PA measurements at different depths are performed in chicken breast to mimic *ex-vivo* testing in biological tissues. As shown in Figure 4-8a,

a piece of black tape is placed underneath the chicken breast to serve as the target. The PAS probe is placed onto a piece of chicken breast, with its tip gently touching the surface of the chicken breast. Figure 4-8b shows the received PA signals at three different depths (t) of 0 mm (black), 1.50 mm (red), and 2.50 mm (green), respectively. Upon excitation of laser pulses, the PA signal from the black-tape target travels through the chicken breast tissue and the optical fiber and reaches the transducer after a certain amount of time. The first positive or negative peak of the recorded PA voltage represents the original PA response. After impinging on the transducer, the PA signal could induce some secondary resonant responses on the transducer, which manifest themselves as lower-frequency oscillations at later times.

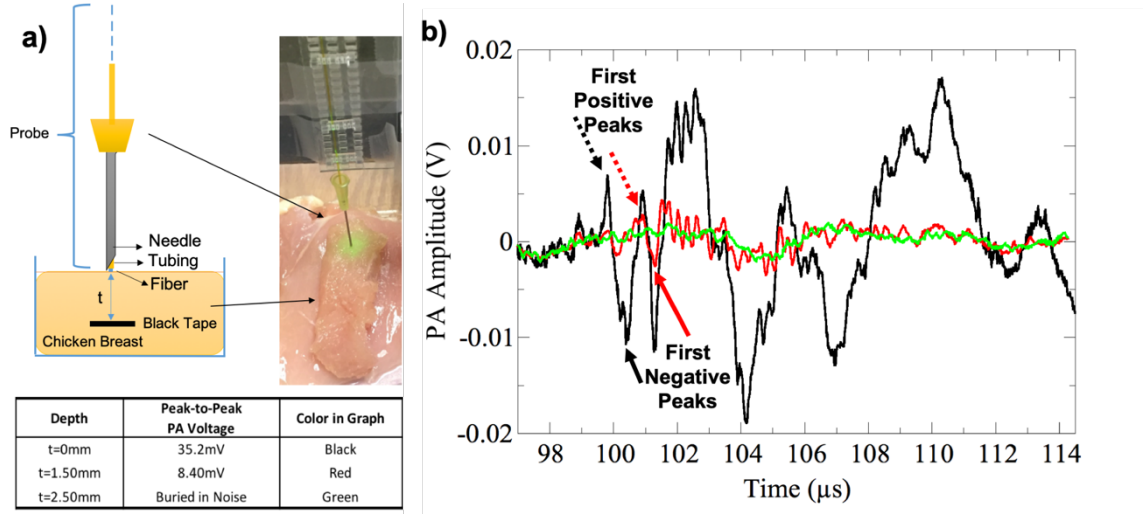

Depth	Peak-to-Peak PA Voltage	Color in Graph
t=0mm	35.2mV	Black
t=1.50mm	8.40mV	Red
t=2.50mm	Buried in Noise	Green

Figure 4-8 PA *Ex-vivo* Tests with Chicken Breast a) Testing Setup and b) PA Signals from Different Depths.

The PA signal amplitude drops when the thickness of the chicken breast increased, which is mainly due to lower optical fluence caused by stronger light diffusion at a larger depth. At t = 2.5 mm, the PA signal started to be buried into noise, indicating the maximal detection depth under the current testing condition. Based on the chicken breast's acoustic velocity, the depth of the target was estimated from the time delay difference between the corresponding positive or negative peaks of the PA signals between the two measurements (0 mm (red) and 1.5 mm (black)). As shown in Figure 4-8b, the delay time difference of the two first positive and negative peaks of the PA signals from the target at 0 mm and 1.5 mm is 1.2 μs and 0.96 μs, respectively. Assuming the acoustic velocity of the chicken breast is 1540 m/s, the estimated depth is 1.77 mm and 1.48 mm, respectively, which match the actual depth (1.5 mm) of the black tape target.

5. PHOTOACOUSTIC SENSING PROBE BASED ON SILICON ACOUSTIC DELAY LINES

So far, new PAS probe designs based on optical-fiber ADLs have been investigated [81, 89]. Due to low acoustic velocity (e.g., ~5000 m/sec) and high acoustic attenuation of fused silica (e.g., ~0.1dB/μsec) [71], the maximal single-mode acoustic transmission frequency and bandwidth of optical-fiber ADLs are typically limited to a few MHz (based on the multimode fused-silica optical fibers). The low acoustic transmission frequency and bandwidth result in poorer depth resolution of PA detection. It can also limit the detection sensitivity because the peak amplitude of the PA signal oftentimes occurs at much higher frequencies.

To address this issue, a new PAS probe design based on SADLs is presented. Compared with fused silica, single-crystalline silicon has lower acoustic attenuation and much higher acoustic velocity (e.g., ~8000 m/sec). It is also compatible with different micromachining methods [72]. Therefore, it is possible to make SADLs with single-mode non-dispersive acoustic transmission frequency much higher than that of optical fibers. Micro linkers fabricated with high-resolution 3D printing are used to maintain the mechanical stability of the probe structure without affecting the acoustic transmission through the SADLs. For demonstration, a prototype SADL-PAS probe has been designed, fabricated, and tested with different concentrations of black dye solutions and biological tissues with an embedded target.

5.1. Probe Design and Construction

Figure 5-1 shows the schematic design of the PAS probe. The optical fiber for light delivery is located at the center of the probe. The SADLs are laid in parallel with the optical fiber. Their acoustic time delay is longer than the duration of the interference signals, such that the PA signal from the target can be easily distinguished. To reduce the overall diameter of the PAS probe, the two SADLs are arranged close together on one side of the optical fiber. The micro linkers hold the optical fiber and the SADLs in position while providing acoustic isolation between them. A "hollow" UTX consists of a flat piezoelectric substrate with a drilled hole to allow the optical fiber to pass through. The diameter of the hole is slightly larger than that of the optical fiber, such that the ends of the surrounding SADLs can have good contact with the UTX. Alternatively, an optically-transparent transducer and two sections of optical fibers can be used [89]; however, the fabrication of the transparent transducer requires special piezoelectric substrate and electrode materials. Light coupling loss can also occur at the optical fiber and transducer interface. Therefore, the "hollow" transducer configuration provides a better solution for the PAS probe design.

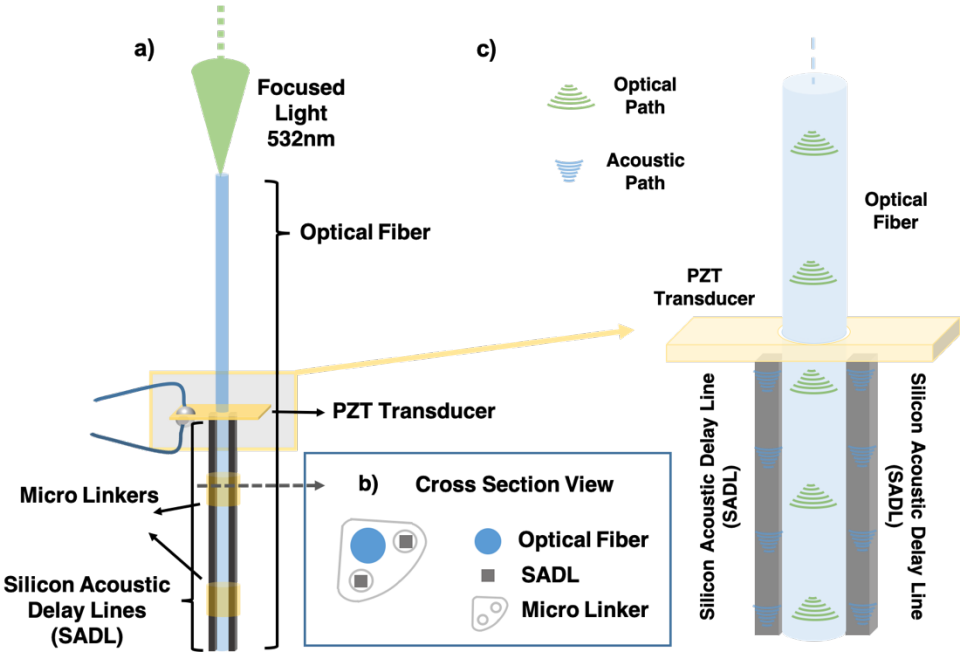

Figure 5-1 a) Schematic of Proposed SADL-PAS Probe, b) Cross-section View, and c) Zoom-in Sketch for Showing the Optical and Acoustic Paths along the Probe.

5.1.1. Optical Fiber for Light Delivery

The optical fiber for light delivery is a fused-silica multimode optical fiber (FT200UMT, THORLABS, Newton, NJ) with a core diameter of 200 µm, a clad layer of 12.5 µm, and an overall diameter of 225 µm. The 200-µm core diameter allows the transmission of micro-joule (µJ) laser pulses without damaging the fiber tip. Because the optical fiber and the SADLs are arranged side by side, there is an offset of the light delivery and the PA detection, resulting in lower PA detection efficiency. To address this issue, the distal end of the fiber is polished at an oblique angle to form a beveled-tip for deflecting a larger amount of light toward the center location of the two SADLs. Optimizing the polishing angle (alpha) of the beveled-tip therefore helps to improve the

sensitivity of the probe [90, 91]. A ray-tracing simulation is conducted to determine the optimal polishing angle of the beveled-tip. As shown in Figure 5-2, the ray-tracing results indicate that a larger amount of light is directed onto the active region, which is the overlapped region for the detected PA signals and optical signals. When the polishing angle of the beveled-tip reaches 34° – 42°, the total number of rays deflected toward the center of the two SADLs is actually close to the total number of rays right in front of a flat-tip (Figure 5-2e).

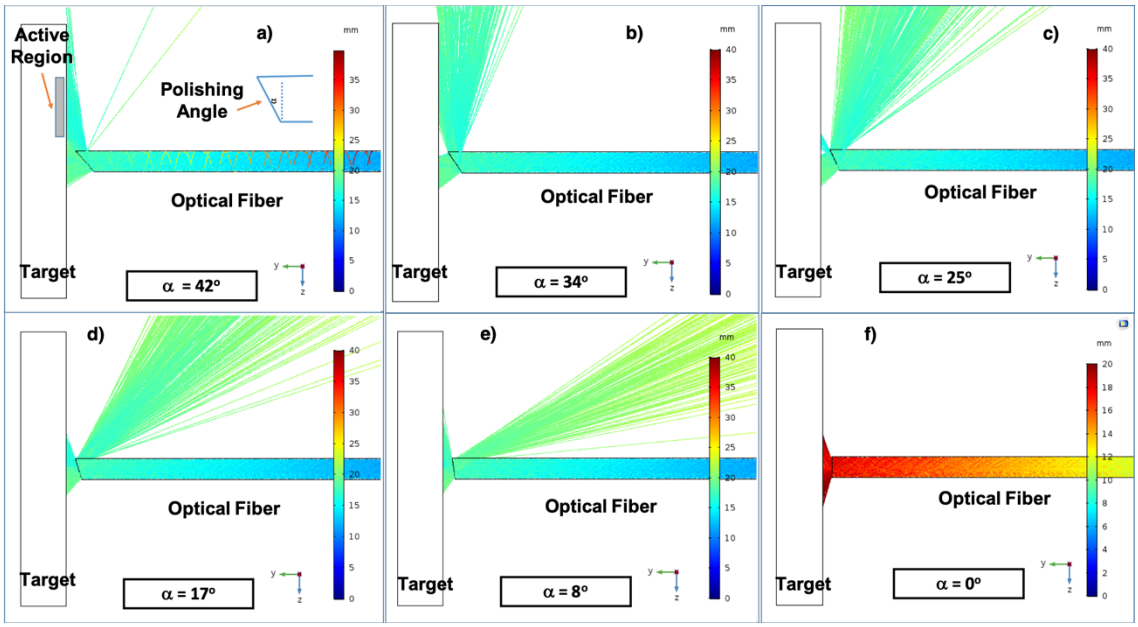

Figure 5-2 Ray-Tracing Simulations for Different Polishing Angles (α) of the Beveled-Tip: a) α = 42°, b) α = 34°, c) α = 25°, d) α = 17°, e) α = 8°, and f) α = 0°.

The beveled fiber tips are prepared using a thin dicing blade (Asahi Diamond, West Chester, OH) with an oblique dicing pattern. The polishing angle should be adjusted to keep the incident angle to normal less than the critical angle, which is 43.3° for the silica-

air interface. Therefore, only the results with angles less than the critical angle are considered in the simulation.

5.1.2. Silicon Acoustic Delay Line

Two wire-type silicon wires with a length of 25-mm and a cross-section of 100 μm × 100 μm are used as SADLs to receive the PA signals. They are diced from a 4-inch 100-μm-thick {100} silicon wafer. The 25-mm length of the SADLs gives an acoustic time delay of ~3μs (assuming an acoustic velocity of ~8400 m/s for silicon), which is longer than the typical duration of the interference signals during excitation, such that the real PA signal from the target can be easily distinguished [81]. For wire-type ADLs, the non-dispersive longitudinal single-mode transmission frequency is limited by its cross-sectional dimension [69, 77, 92-94]. The highest frequency of single-mode transmission is usually around 0.1~0.2 c/d, where c and d are the acoustic velocity and the cross-sectional dimension (width or thickness), respectively. With a 100 μm × 100 μm cross-section, the highest single-mode transmission frequency of the SADL is estimated to be ~17 MHz.

5.1.3. Ultrasound Transducer

For receiving the PA signals through the SADLs, a 160-μm-thick PZT ceramic disc (Type VI, APC International Ltd., Mackeyville, PA) is used as the piezoelectric substrate of the UTX, which has a thickness-mode resonance frequency of ~13 MHz. The PZT disc was diced into small pieces (5.0 x 2.0 mm^2) to reduce the parasitic capacitance of the transducer. An alignment hole and a spare hole were drilled to allow the optical fiber to pass through. The hole diameter is about 430 μm, which is slightly larger than the

diameter of the optical fiber (core + cladding). This provides a less-contacted lateral surface of the optical fiber to the transducer and accordingly creates less acoustic crosstalk. The optical fiber is subsequently inserted through the hole and fixed so that misalignment issues between optics and the optical fiber are resolved. In this configuration, the transducer no longer blocks the light and maintains the contacts with the SADL. To facilitate the wiring, two chromium/copper contact pads (one on the top and one on the bottom) were deposited onto the PZT substrate by e-beam evaporation. The PZT substrate was fixed onto a glass pad (also coated with two matching electrodes). Transducer mounting was completed by connecting an SMA connector to the glass-transducer assembly. No matching layer was added between the PZT transducer and the SADLs because the acoustic impedances of silicon and the PZT are close to each other (Figure 5-3).

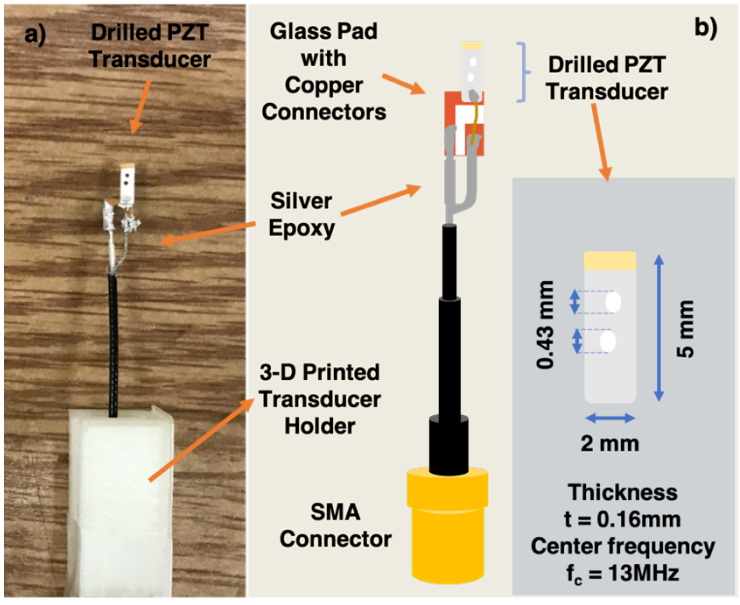

Figure 5-3 Transducer Assembly a) Photo and b) Side View Diagram.

5.1.4. Micro Linkers

Two micro linkers are used for fixing the optical fiber and two SADLs together in a stable position. Previously, sub-millimeter-size polymer holders have been used as a solution to overcome the issue of mechanical protection of SADLs [80]. In this work, to achieve the required resolution, a high-resolution 3-D printer (NanoScribe Photonics Professional GT2, Germany) was used for printing the micro linkers with a resolution of 5 μm (Figure 5-4). The overall diameter and length of the micro linker is 700 μm and 2 mm, respectively. To prevent acoustic leakage due to direct contact, the alignment holes for SADLs are formed into a circular shape with a diameter of 200 μm to reduce the contact area between the micro linker and SADLs. The alignment hole for the optical fiber has a diameter of 350 μm, which is slightly larger than that of the optical fiber (after the jacket layer is removed for space saving). In the alignment hole for the optical fiber, four small protruding structures were added to create a tiny gap between the optical fiber and the micro linkers for further increasing the acoustic isolation.

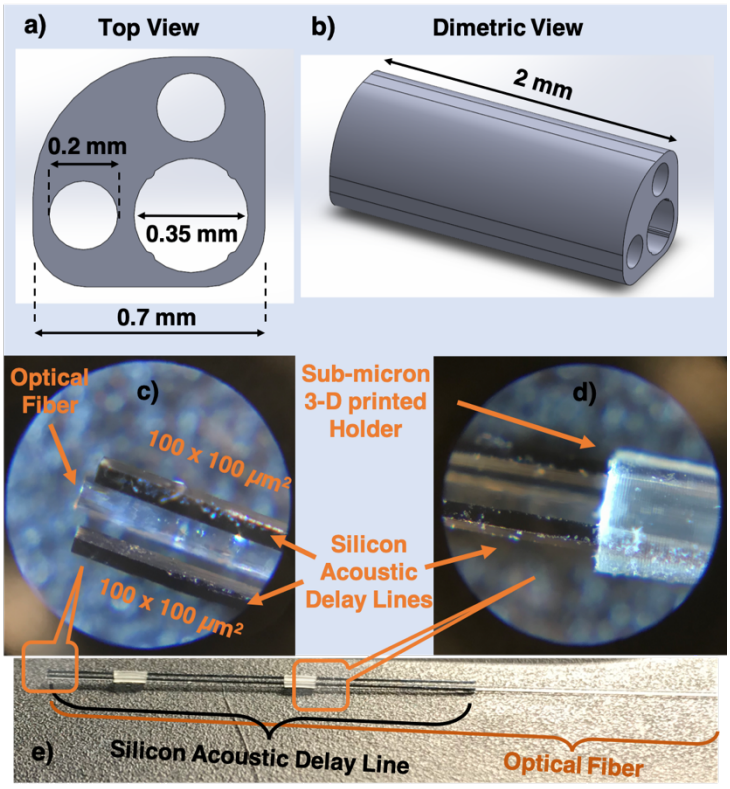

Figure 5-4 Micro Linkers: a) Schematic Top View, b) Schematic Prospective View, c) Photo of Assembled Probe Tip, d) Photo of a Micro Linker with the Optical Fiber and SADLs Assembled, and e) Global View of the Probe Assembly with Micro Linkers.

5.2. Testing and Characterization

5.2.1. Ultrasound Transmission through SADL

The ultrasound transmission through an SADL is characterized using two-port ultrasound testing (Figure 5-5a). The SADL is placed between two UTXs (V250, Olympus NDT, Waltham, MA, USA). Mineral oil is applied onto the contacts between the ends of SADLs and the surfaces of transmitting & receiving transducers to enhance coupling efficiency and minimize unwanted reverberation. The pulser/receiver (5072PR, Olympus

NDT, Waltham, MA) was set to the transmission mode, which sent a driving voltage pulse to the transmitting transducer to generate ultrasound signals and also amplified signals detected by a receiving transducer. Each received ultrasound signal was averaged 64 times and recorded on a digital oscilloscope (TDS2002C, Tektronix Inc., Beaverton, OR, USA) to determine their peak amplitude and time delay.

Figure 5-5b shows the received ultrasound signal after traveling through a SADL with a length of 25 mm. The signal arrives at the receiving transducer after a time delay, which is 3.080 µs. The average acoustic velocity of SADLs is determined to be ~8120 m/sec. Fig. 5-5b also indicates the frequency spectrum of the received ultrasound signal after FFT. The peak frequency is around 14.2 MHz with 17% bandwidth. This result indicates that the coefficient of the single-mode transmission frequency (*c/d*) is close to 0.2.

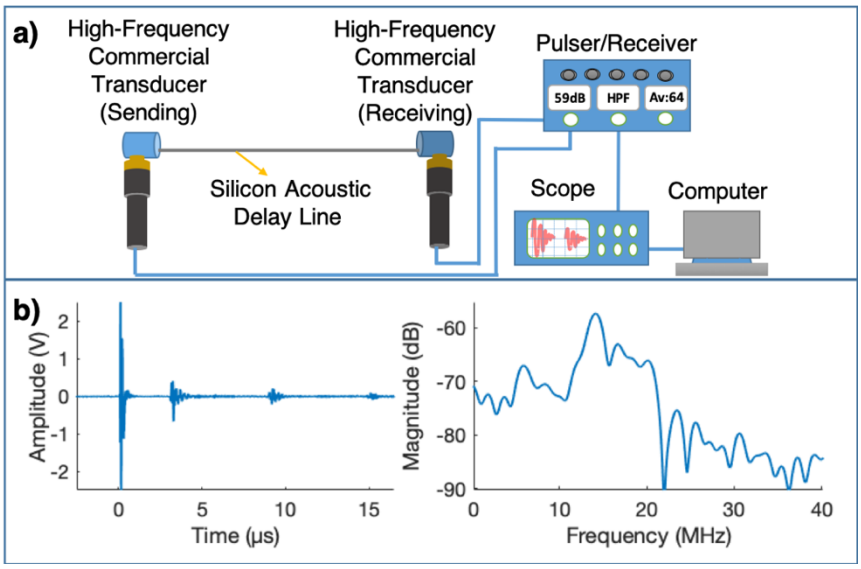

Figure 5-5 Acoustic Characterization of Single SADL: a) Two-Port Ultrasound Testing Setup, and b) Time-Domain Signal and FFT Spectra.

5.2.2. PA Transmission through SADL

In the PA verification test (Figure 5-6), different acoustic time delays for different vertical laser beam distance to the transducer (L1, L2, and L3) have been tested. The testing setup for a thin silicon line (100 µm x 100 µm) is shown in Figure 5-6a and Figure 5-6c. An average acoustic velocity of silicon can be calculated using those three PA test results, which are close to the typical acoustic velocity of silicon (Figure 5-6b). Vertical PA test results show that there are received signals matching with the theoretical acoustic time delays transmitted through the thin silicon line (Figure 5-6d) and also FFT of the PA tests, which provides similar high-frequency transmission spectra for different laser beam locations.

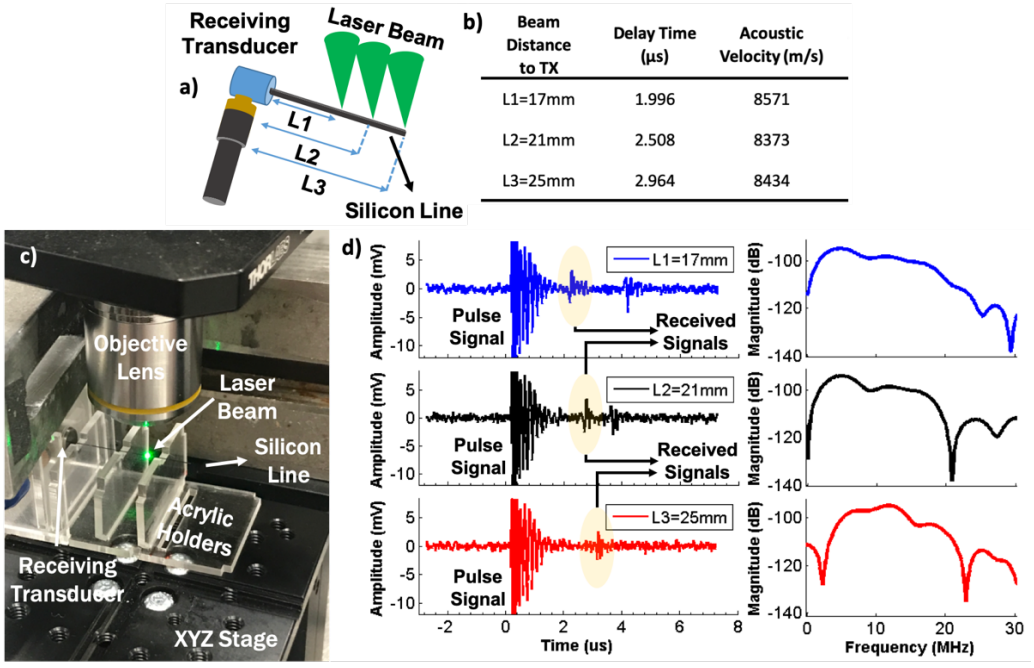

Figure 5-6 Vertical PA Tests for a Thin Silicon Line a) Vertical Installation, b) Acoustic Properties of Different Test Points, c) Photo of the Testing Setup and d) Test Results for Different Laser Beam Locations.

5.2.3. PA Characterization

The PA detection capability of the PAS probe is characterized with a test setup shown in Figure 5-7a. The light source is an Nd:YAG laser (SPOT-10-200-532, Elforlight Ltd, Northants, UK) operating at a wavelength of 532 nm. The duration of the light pulse is 1.75 ns, and the maximum output energy is 20 μJ per pulse. The pulse repetition rate is 2 kHz. A three-axis stage and 3-D printed the main holder are used during the PA testing (Figure 5-7b). A black vinyl electrical tape serves used as the target. The received PA signal was amplified by the internal voltage amplifier of the Pulser/Receiver (5073PR, Olympus NDT, Waltham, MA, USA). The amplified PA signal is received by a digital oscilloscope with a sampling rate of 100MHz.

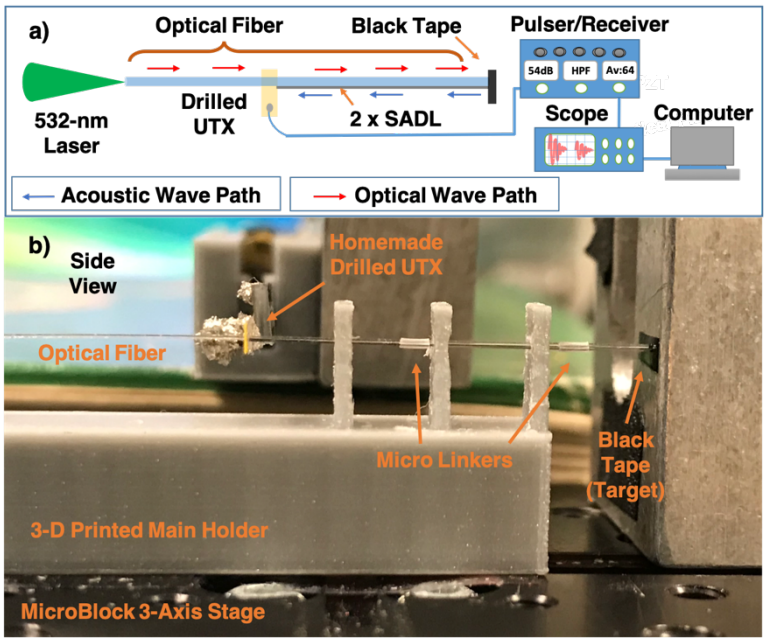

Figure 5-7 PA Testing Setup of SADL-PAS Probe: a) Schematic and b) Photo.

Figure 5-8a shows a received PA signal from the black tape target. It has a similar time delay (3.080 µs) and frequency spectrum (center frequency of 15.1 MHz with 14% bandwidth) of the received ultrasound signal (Figure 5-8b). The acoustic bandwidth is slightly narrower, which is generally due to the smaller bandwidth of the homemade PZT transducer. For probe characterization, different laser power levels are used to reveal the relationship between the optical fluence and the resulting PA signal strength (Figure 5-8c). The laser pulse energy and the optical fluence are determined based on the measured laser power, the pulse repetition rate, and also the estimated illumination area while other properties of PA signal generation (Grüneisen coefficient and the absorption coefficient) remain the same [95]. At the probe tip, the maximal pulse energy was 7.77 µJ/pulse and the maximal optical fluence was 19.54 mJ/cm^2, which is below the ANSI (American National Standard Institute) safety limit of 20 mJ/cm^2 [32]. As shown in Figure 5-8c, the PA voltage and SNR increase with the optical fluence with a strong linear correlation (R^2 = 0.9714 and R^2 = 0.9946).

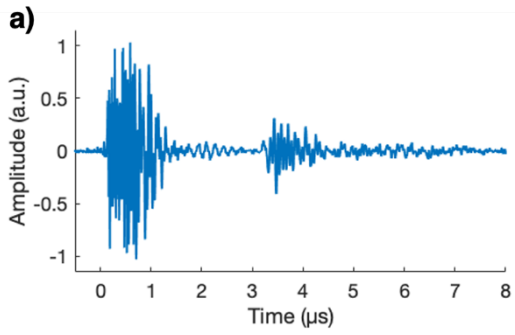

Figure 5-8 a) Received Time-Domain PA Signal (~ 3µs), b) FFT Spectra of the PA Signal, and c) PA voltage and SNR vs. Optical Fluence.

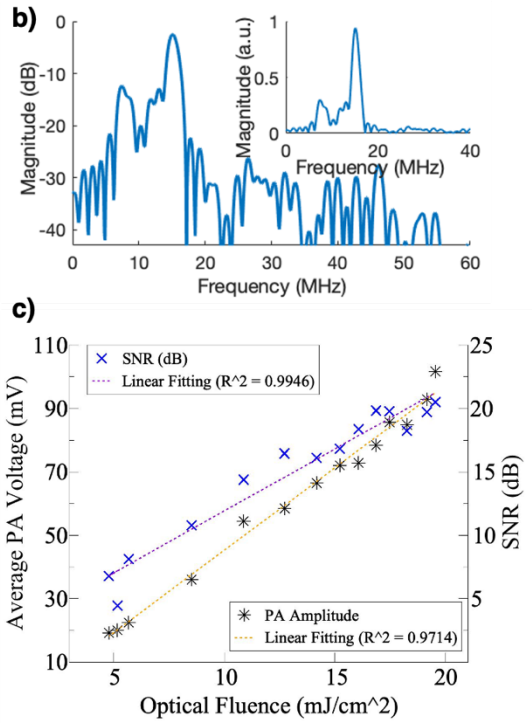

Figure 5-8 Continued.

5.2.4. Dye Concentration Characterization

The identical PA testing setup (Figure 5-7) is used for the dye concentration characterization. Dye solutions are prepared with black dye powder by diluting with DI water to reach the desired concentration. The dye solution is transferred into a PVC tubing with a syringe and the 3-axis stage is gradually moved towards the tubing until the probe mounted onto the stage and the dye solution have contacted.

For each dye concentration, five different PA tests are performed. The average PA peak voltage with the standard deviation is shown in Figure 5-9. There are in total of fourteen concentration data (n=14) are tested starting from 0.001 g/ml to 0.05 g/ml. There exists a strong linear correlation between the PA peak voltage and dye concentration

(R^2 = 0.934). When the black dye concentration was reduced from 0.05 g/ml to 0.001 g/ml, the PA amplitude changes from 39.2 mV to 8.2 mV and SNR also changes from 13.78 dB to 2.36 dB. The PA amplitude results determine the detection limit of about 0.001 g/ml for the SADL-PAS probe with the black dye solution as the target.

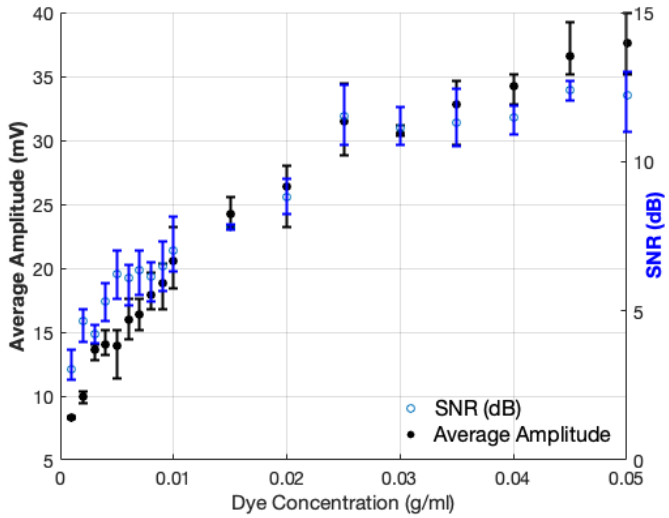

Figure 5-9 PA Characterization with Different Black Dye Concentrations.

5.2.5. Target Detection in Biological Tissues

The capability of the SADL-PAS probe for *in-vivo* sensing in biological tissues is demonstrated by utilizing chicken breast as the testing medium (Figure 5-10a). A 3-D printed container is used to hold the two layers of chicken breast in place. One layer is laid in the container first. The target (a piece of black tape) is placed onto this first layer and the second layer topped the target (Figure 5-10b). Figure 5-11 shows the acquired PA signals from the black tape target at different depths (d_1, d_2, d_3, and d_{max}) (Figure 5-11a-

d). The amplitude of the PA received signal attenuates when the depth of the target increases because there is a lower optical fluence occurred by stronger light diffusion at larger depths. After going deeper thicknesses than d = 1.51 mm, the PA signal started to be buried into noise, which shows the maximal detection depth under the current testing condition. Based on the time delay in tissues, the depths are estimated by utilizing three time points: zero intersection, first positive peak, and first negative peak (Table 5-1). Figure 5-11e shows frequency spectra of the received PA signal from the black tape target at different depths. It is clear that the SADL-PAS probe functionally has high acoustic transmission frequency even at larger depths (center frequency of ~15 MHz, which is similar to the center frequency of PA characterization result of the probe).

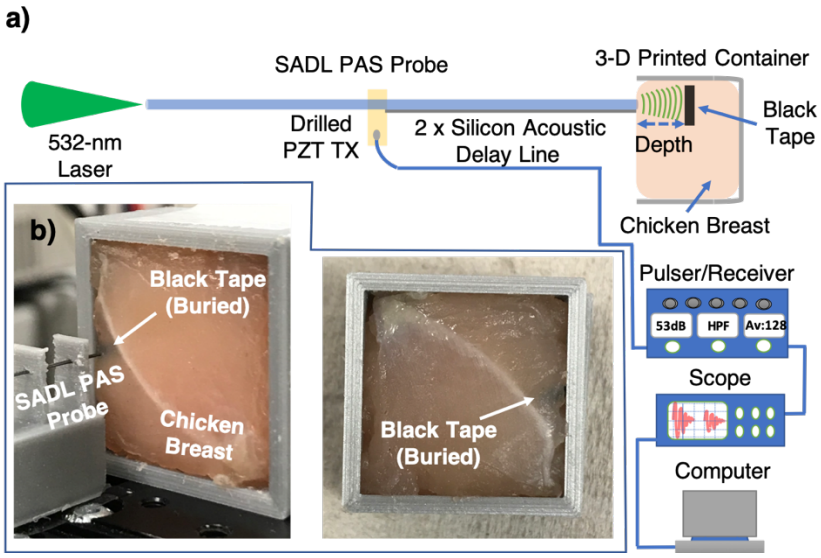

Figure 5-10 PA Test in Chicken Breast a) Testing Setup and b) Photo of Buried Target and Chicken Breast Medium.

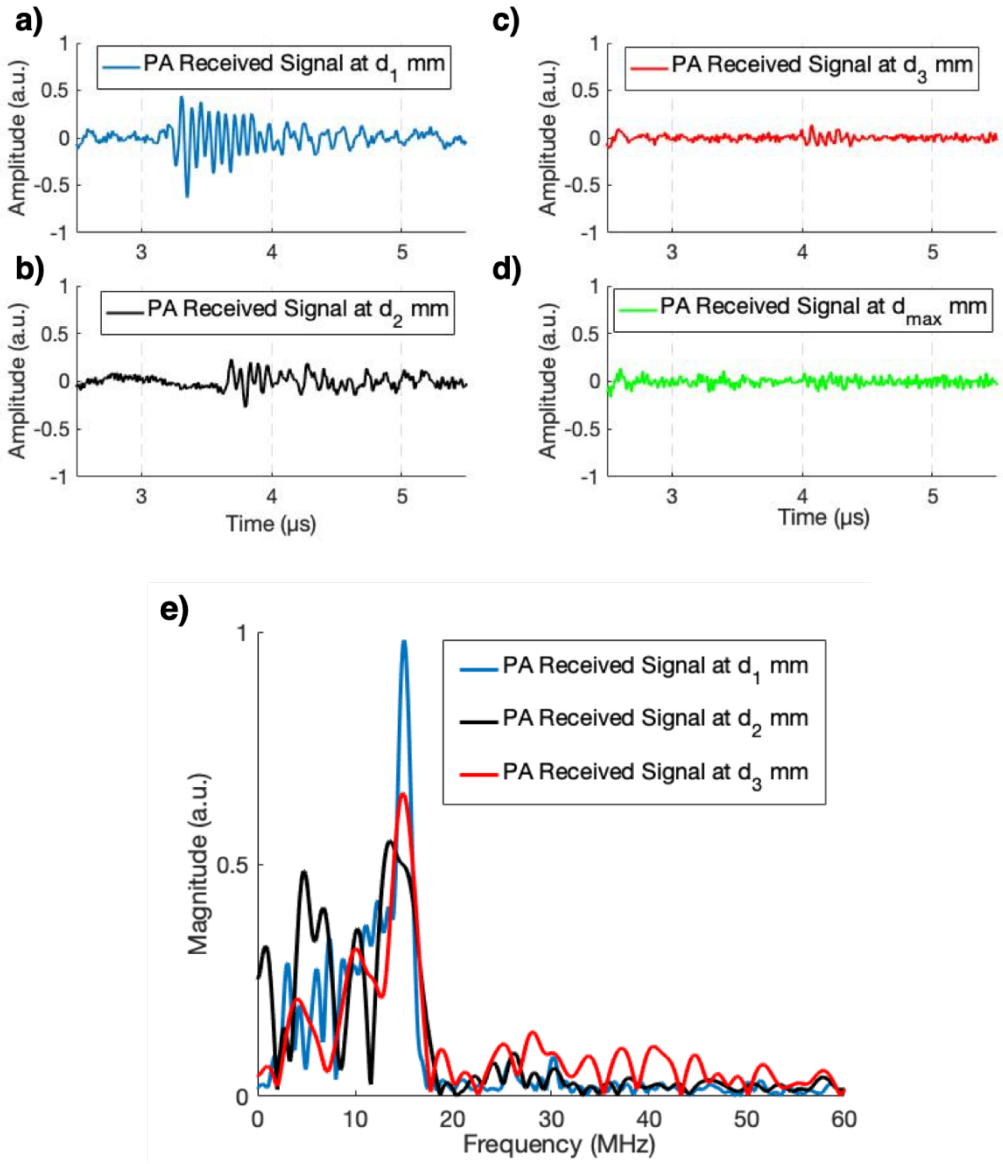

Figure 5-11 Received PA Signals from the Target at Different Depths a) d_1 = 0mm, b) d_2 = 0.8mm, c) d_3 = 1.34mm, d) d_{max} = 1.51mm, and e) FFT spectra.

To determine the average depth, the reference time delay is determined when the black tape is placed on the top of the chicken breast (d_1 = 0 mm) and only the time delay of the SADL is considered. The acoustic time delay in the chicken breast tissue between

the probe tip and the black tape target is calculated by subtracting the time delay of the SADL (~3.060 μs) from the total time delay. Assuming the acoustic velocity of the chicken breast is ~1540 m/s [96], the distance between the probe tip and the black tape target is estimated based on the calculated time delay in the chicken breast tissue, which matches with the actual thickness of the chicken breast piece.

Table 5-1 Time Points of The First Peaks in The PA Signals and the Calculated Target Depth.

Depth	Zero Intersection (μs)	First Positive Peaks (μs)	First Negative Peaks (μs)	Calculated Average Depth
d_1	3.060	3.120	3.168	0 mm
d_2	3.580	3.628	3.692	0.797 mm
d_3	3.939	3.966	4.012	1.338 mm
d_{max}	4.063	4.100	4.122	1.508 mm

5.3. Discussion

A PAS probe with SADLs capable of working at high frequencies has been demonstrated. The SADL components are specifically designed to receive higher frequency signals and to make a compact PA probe design. Theoretically, a higher acoustic frequency range can be obtained by further shrinking the cross-sectional dimension of the SADLs, which also reduces both the mechanical strength and the

acoustic detection sensitivity. This issue could be alleviated by increasing the number of SADLs. Nevertheless, as the SADLs become more fragile, their handling and assembly will become more challenging. New micromachining process is needed to address this challenge, which is partially covered in the next section.

6. MICROMACHINED SILICON ACOUSTIC DELAY LINES FOR HIGH-FREQUENCY ULTRASOUND TRANSMISSION

This section presents a new micromachined silicon acoustic delay line (SADL) design to overcome the structural instability issue in SADLs, especially for high-frequency operations. Both the simulation and experimental results show that the new SADL design can significantly increase the mechanical stiffness of the SADL structure without degrading its acoustic performance. With the use of a novel thin film back-side linker, the SADL can be used for easy handling and assembly. It can be scaled up and down to provide different ultrasound frequency and time delay. For demonstration, high-frequency ultrasound transmission through a multi-channel SADL array has been achieved. The new high-frequency SADL design is expected to enable multi-channel PAS capability at high frequencies. It could be also useful for building new PA and ultrasound imaging systems with less hardware complexity.

6.1. Design and Verification

6.1.1. Design Principles

In PA or ultrasound imaging, 1D or 2D transducer arrays with multi-channel data acquisition (DAQ) electronics are used to receive the ultrasound signals from the target for image reconstruction (Figure 6-1a). To improve the imaging resolution and speed, a larger number of transducer elements and DAQ channels operating at higher ultrasonic frequencies are required, which however will make the ultrasound system more complex, power-consuming, and costly. This issue could be alleviated by using an ADL array to

add suitable time delays into the ultrasound and force them to arrive at a (single element) receiving transducer at different times. As a result, all of the ultrasound signals for image reconstruction can be properly received with only one transducer interfaced with a single DAQ channel (Figure 6-1b). The capability to combine multiple signal channels into "single" could significantly reduce the complexity, power consumption, and cost of the ultrasound imaging systems.

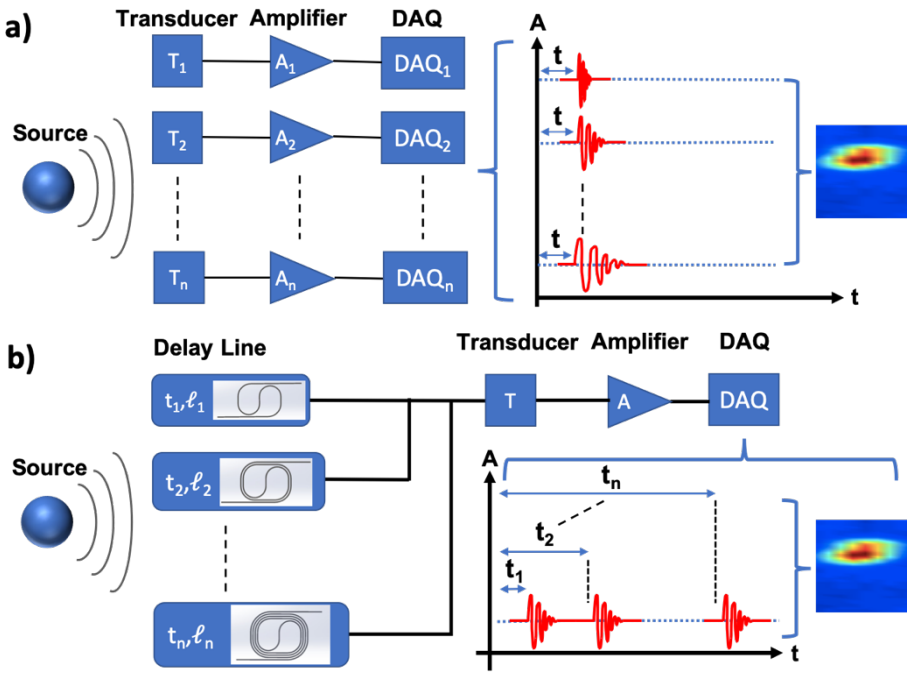

Figure 6-1 Ultrasound Data Acquisition and Image Reconstruction: a) Using a Transducer Array and a Multi-channel DAQ System and b) Using an ADL Array Interfaced with a Single Element Transducer and Single-channel DAQ system.

As discussed in Section 5, due to its excellent mechanical properties, high acoustic velocity, low acoustic attenuation [76], and ease of micropatterning, single-crystalline

silicon can be an ideal constituent material for making ADLs, especially for high-frequency operations. In ultrasound imaging, the typical duration of an ultrasound signal is a few microseconds. To temporally separate multiple ultrasound signals, the length of an ADL could reach tens of centimeters for providing sufficient acoustic time delay. To accommodate such a large length on a small substrate, SADLs are usually laid out as double-wound spiral coils (coil-shaped) [72, 73].

In a coil-shaped SADL design, the amplitude of the ultrasound signal increases when the radius of curvature increases. Also, some of the waves will be reflected back if we keep the bending radius small [72, 73]. Since the mode conversion and the direct reflection result in reductions in the amplitude of the received acoustic signal for bending portions, the radii of curvature have to be made much larger than the longest wavelength. The highest transmission frequency of a SADL is inversely related to the size of its cross-section [69, 71, 89] based on the relationship,

$$d/\lambda = d\,f/V_0 \ll 1 \tag{6.1}$$

where d is the width or thickness of the SADL (whichever is smaller), λ is the ultraosund wavelength, f is the ultrasound frequency, and V_0 is the acoustic velocity of the first longitudinal mode in silicon. For example, for ≥ 10 MHz operations, the cross-section of the SADL will need to be ≤ 100 μm × 100 μm, but the large length and small width/thickness make the SADL structures extremely soft. They can be easily deformed and even fractured under their self-weights, which poses a big challenge in their handling and assembly into an array.

6.1.2. Acoustic and Mechanical Design

Figure 6-2 shows the schematic of the new SADL design. It consists of a coil-shaped delay line structure at the center and a surrounding frame for protection and handling. Both the delay line structure and the surrounding frame can be formed on the same silicon substrate in one patterning step. Two zig-zag isolation trenches are created in the frame to block ultrasound signals leaking into the frame from reaching the output terminal. One fundamental challenge in the SADL design is how to link all the isolated structures together into a single piece with good mechanical stability while maintaining the acoustic isolation between them. Although (discrete) micro linkers (made of silicon or other materials) can be deployed at specific locations inside the isolation trenches, they will inevitably create unwanted connection points and therefore higher acoustic attenuation and crosstalk.

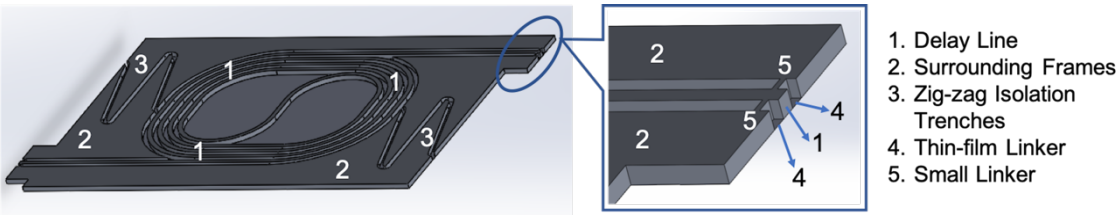

Figure 6-2 Schematic of the new SADL design.

To address this issue, a continuous thin film made of materials with low acoustic attenuation can be deposited onto the backside of the SADL substrate. Due to its extremely small thickness and also the fact that it only contacts the bottom surface of the SADL, the acoustic attenuation and crosstalk caused by the thin-film linker can be minimized.

Secondly, when combined with zig-zag isolation trenches, the thin-film linker can significantly enhance the mechanical stiffness along all (x/y/z) directions. If necessary, two small (discrete) linkers can be added to the input and output terminals, respectively, to further increase the structural robustness. Because they are located at the two terminals with small sizes, the crosstalk caused by the discrete linkers is minimized. In this work, aluminum is chosen as the material for the thin-film linker. It has low acoustic attenuation and intrinsic stress and is also resistant to silicon plasma etching. For verification, the structural deformation of the new SADL design under an in-plane and out-of-plane acceleration of 10 g was simulated (Figure 6-3). The simulation results show that the SADL structure has very little deformation, which indicates its high mechanical stiffness.

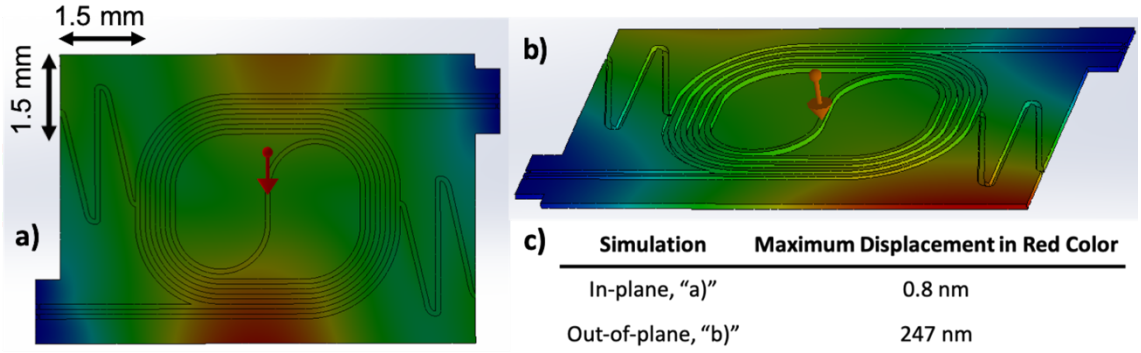

Figure 6-3 Finite-Element Simulation Results of The Deformation of an SADL Structure: a) Under an In-Plane Acceleration of 10 g, b) Under an Out-of-Plane Acceleration of 10 g, and c) Maximum Displacements in Red Color. Note: The thickness of the substrate and the width of the delay line are both 100 µm, and the red arrows in "a)" and "b)" shows the direction of acceleration.

6.2. Fabrication and Testing

6.2.1. Single SADL

To verify the acoustic performance of the new SADL design, a single four-turn SADL was fabricated and tested. The width of the delay line is 100 μm and the total delay length is 63.2 mm. The fabrication is conducted on a 100-μm-thick and double-side polished {100} silicon wafer. A 300-nm-thick aluminum layer is evaporated onto the front side and patterned to serve as the hard mask for silicon etching. A 1-μm-thick aluminum layer was evaporated onto the backside as the thin-film linker. The silicon etching is conducted by using a cryogenic process. The cryogenic silicon etching does not generate completely vertical sidewalls. Therefore, after the silicon etching, a small section of the input and output terminals are diced to form a flat and smooth end surface, which provides better contacts with the UTXs during the testing.

Two-port ultrasound transmission testing is conducted to characterize the acoustic performance of the fabricated SADL. During the testing, the input and output terminals of the SADL are contacted onto the surface of the transmitting and receiving transducers, respectively. The ultrasound (pulse) signal generated by the transmitting transducer travels through the delay line and reaches the receiving transducer. To evaluate the influence of the aluminum thin-film linker on the ultrasound transmission, the two-port ultrasound transmission testing was repeated on the same SADL: 1) after the surrounding frames removed, and 2) after the surrounding frames removed and the entire aluminum layer etched away (Figure 6-4).

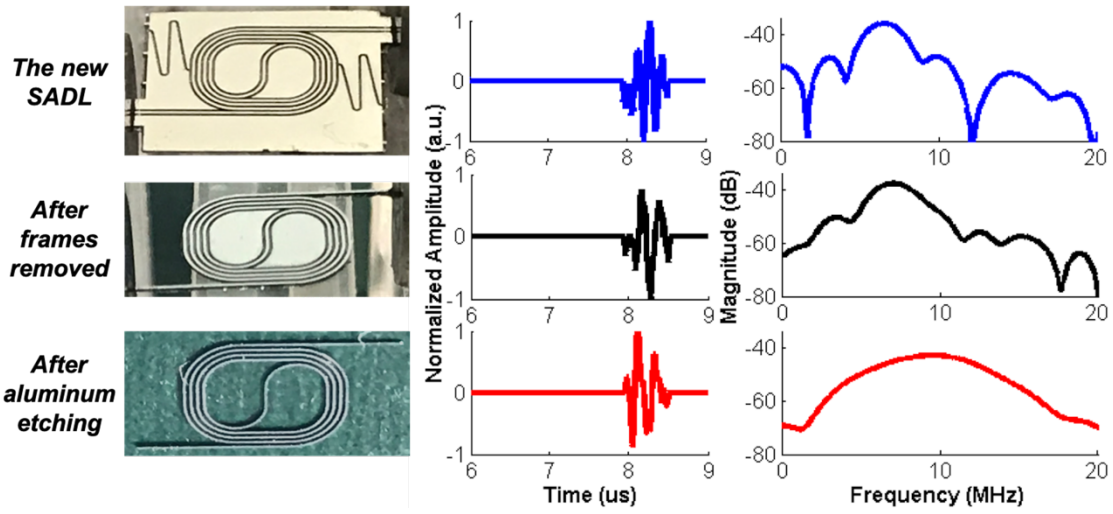

Figure 6-4 Fabricated SADL, Received Time-Domain Ultrasound Signals, and Their Frequency Spectra From: Top – The Complete SADL, Middle – After Frames Removed, and Bottom – After Frames Removed & Aluminum Linker Etched.

As shown in Figure 6-4, both the amplitude and the time delay of the first positive peak in the three cases are almost identical. The time delay is around 7.9 μs, which matches the theoretical value calculated by dividing the delay length by the nominal acoustic velocity of the first longitudinal mode silicon. In all three cases, the 20-dB (high) cut-off frequency of the transmitted ultrasound signals is ~17 MHz, which is close to that predicted from Equation (1). This result shows that only the ultrasound signals that travel along the delay line can reach the receiving transducer. The acoustic isolation between the adjacent turns of the delay line and that between the delay line and the surrounding frame is well maintained. Therefore, the aluminum thin-film linker does not create significant attenuation and crosstalk for the ultrasound transmission. It should be noted that there exist slightly stronger ripples in the ultrasound signal received from the complete SADL structure. This is possibly due to the different contact conditions between the delay line

terminals and the two transducers. The existence of the ripples makes the frequency spectra (from FFT) appear slightly different.

6.2.2. Multi-Channel Delay Line Arrays

For demonstration, a four-channel SADL array is designed, fabricated, and tested. To facilitate the assembly, all four SADLs share the same outer shape and dimensions (see Figure 6-2). Table 6-1 lists the main design parameters of the SADL array.

Table 6-1 Design Parameters of Four-channel SADL Array.

Parameters	Value
Outer Dimension	5.9 mm x 9.3 mm
Cross Section	100 μm x 100 μm
The gap between adjacent turns	100 μm
Number of turns	1, 2, 3, 4
Delay Length (mm)	21.5, 34.1, 48.1, 63.2
The acoustic velocity of silicon (m/s)	8430
Expected time delay (μs)	2.55, 4.05, 5.70, 7.50

The four SADLs are stacked together onto a 3D-printed main holder with two posts for better aligning the input and output terminals. To ensure acoustic isolation, a polyethylene terephthalate (PET) film spacer is inserted between two adjacent SADLs. (Figure 6-5a). Two-port ultrasound testing was conducted to characterize the ultrasound transmission through the SADL array. The ultrasound (pulse) signal generated by the

transmitting transducer travel through the four SADLs individually and reach the receiving transducer with different amount of time delay (Figure 6-5b), which are completely distinguishable from each other. Since non-uniform contact conditions between the SADLs and the two UTXs exist, the amplitudes of the received ultrasound signals do not show a linear trend unlikely acoustic attenuation changes exponentially with the delay length.

The actual time delays (2.60, 4.14, 5.84, 7.85 µs) determined from the time-domain measurement are slightly longer than the predicted values listed in Table 6-1. This can be explained by the fact that as an anisotropic material, the actual acoustic velocity in silicon can differ from its nominal value when the ultrasound signal travels along the (curved) SADL.

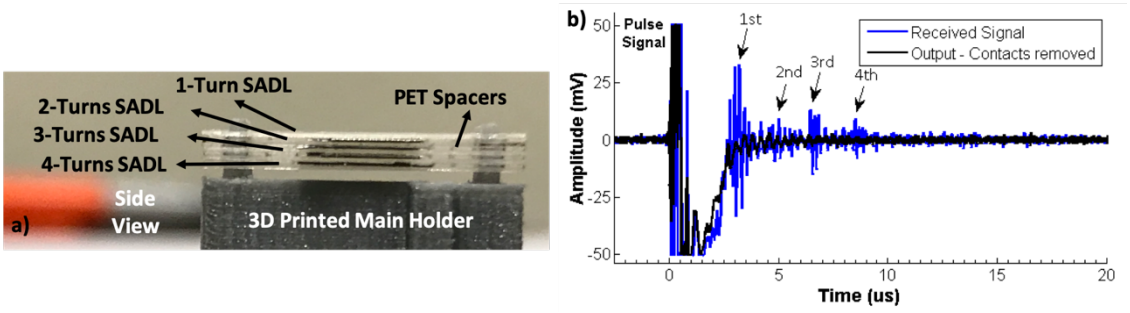

Figure 6-5 a) Side View for an Assembled Four-Channel SADL Array and b) Received Time-Domain Ultrasound Signals When the Input Terminals of The SADL Array Are ON (Blue) and OFF (Black) Contact with The Sending Transducer.

7. CONCLUSION AND FUTURE WORK

In this study, PAS probes using wire-type ADLs are investigated and demonstrated. Different from conventional approaches, the use of ADLs addresses two fundamental challenges in PAS probe design. With suitable time delay, PA signals will be forced to arrive at the receiving ultrasound transducer (UTX) and therefore avoid mixing with the much stronger interference signals. This allows PA measurements to be performed on targets close to or even contacted with the probe. Also, the receiving transducer can be located outside the probe shank. As a result, the diameter of the probe shank can be significantly reduced to minimize its invasiveness especially for *in-vivo* use.

Optical fibers (especially those made of fused silica), which are readily available, can serve as both optical waveguides and ADLs with non-dispersive transmission up to a few MHz. A two-fiber probe design can consist of two optical fibers arranged side-by-side with one for light delivery and the other one for the detection and transmission of PA signals. An even more compact probe design can be obtained by using a single optical fiber for both light delivery and PA reception. To achieve this, an optically transparent UTX will be needed between the optical source and the optical fiber, allowing the light delivery and reception of the PA signals through the same optical fiber. One additional advantage of single optical fiber design is that the light delivery and acoustic detection are automatically aligned with each other, thereby resulting in higher efficiency for PA signal reception.

One potential drawback of optical-fiber delay lines is the low acoustic transmission frequency and bandwidth, which is limited by the low acoustic velocity of fused-silica and also the high acoustic attenuation (at higher frequencies). This is caused by the intrinsic material loss and damping of the cladding and jacket layer. The low detection frequency can result in poor depth resolution and sensitivity, as the peak amplitude of the PA signal could occur at much higher frequencies. This issue can be addressed by using materials with higher acoustic velocity and lower acoustic attenuation. As an almost elastic crystal material, single-crystalline silicon has excellent mechanical and acoustic properties, with much higher acoustic velocity and lower acoustic attenuation than fused silica. Therefore, single-crystalline silicon serves as a better structural material than optical fibers for the construction of the ADLs for PAS probe designs especially for high-frequency operations.

With the recent development of advanced micromachining process, complex silicon microstructures can be directly fabricated on a silicon substrate in one step without intensive manual assembly. This makes it possible to achieve single, multiple and even an array of SADLs for transmitting multi-channel high-frequency ultrasound signals with different time delays. However, due to their extremely large aspect ratio (length vs. width and thickness), SADLs tend to become soft and fragile with very low mechanical stiffness, causing structural instability or collapsing. To address this issue, thin-film backside linkers can be integrated without significantly affecting the acoustic performance. It allows the addition of surrounding frames to the delay line structure for better protection and easier handling. This new SADL and linker design can be easily scaled up or down to

provide different ultrasound frequency response and time delay allowing multi-channel detection capability.

The completion of this work builds a solid foundation for many future efforts. For example, the new PAS probe designs can enable various applications in biomedicine, chemical analysis, material characterization and other areas. With parallel SADL arrays, a simple and low-cost multi-channel ultrasound receiver system can be developed to allow fast data acquisition (DAQ) for real-time PA imaging, especially at high frequencies. In addition, micro actuators can be integrated to enable tunable or switchable acoustic delay line circuits for on-chip signal processing in the acoustic domain, which is expected to provide a new solution for reducing the burden on the DAQ electronics in current ultrasound receivers.

REFERENCES

[1] A. G. Bell, "The photophone," *Science,* vol. 1, no. 11, pp. 130-134, 1880.

[2] A. G. Bell, "The production of sound by radiant energy," *Science,* vol. 2, no. 48, pp. 242-253, 1881.

[3] L. V. Wang, "Prospects of photoacoustic tomography," *Medical Physics,* vol. 35, no. 12, pp. 5758-5767, 2008.

[4] P. Beard, "Biomedical photoacoustic imaging," *Interface Focus,* vol. 1, no. 4, pp. 602-631, 2011.

[5] V. Ntziachristos, "Going deeper than microscopy: the optical imaging frontier in biology," *Nature Methods,* vol. 7, no. 8, pp. 603-614, 2010.

[6] A. Oraevsky and A. Karabutov, "Optoacoustic tomography," *Biomedical Photonics Handbook,* vol. 34, pp. 1-34, 2003.

[7] L. V. Wang, *Photoacoustic imaging and spectroscopy*. CRC press, Boca Raton, Florida, 2009.

[8] J. Yao and L. V. Wang, "Sensitivity of photoacoustic microscopy," *Photoacoustics,* vol. 2, no. 2, pp. 87-101, 2014.

[9] C. Hoelen, F. De Mul, R. Pongers, and A. Dekker, "Three-dimensional photoacoustic imaging of blood vessels in tissue," *Optics Letters,* vol. 23, no. 8, pp. 648-650, 1998.

[10] Oraevsky A. A., Alexander A., Valeri A. Andreev, Alexander A. Karabutov, R. Declan Fleming, Zoran Gatalica, Harbans Singh, and Rinat O. Esenaliev, "Laser

optoacoustic imaging of the breast: detection of cancer angiogenesis," in *Optical Tomography and Spectroscopy of Tissue III*, 1999, vol. 3597: International Society for Optics and Photonics, pp. 352-363.

[11] R. O. Esenaliev, A. A. Karabutov, and A. A. Oraevsky, "Sensitivity of laser opto-acoustic imaging in detection of small deeply embedded tumors," *IEEE Journal of Selected Topics in Quantum Electronics,* vol. 5, no. 4, pp. 981-988, 1999.

[12] X. Wang, Y. Xu, M. Xu, S. Yokoo, E. S. Fry, and L. V. Wang, "Photoacoustic tomography of biological tissues with high cross-section resolution: Reconstruction and experiment," *Medical Physics,* vol. 29, no. 12, pp. 2799-2805, 2002.

[13] M. Kinnunen and R. Myllylä, "Frequency spectrum analysis of pulsed photoacoustic signals in Intralipid," in *Advanced Laser Technologies 2007*, 2008, vol. 7022: International Society for Optics and Photonics, p. 702215.

[14] T. Lister, P. A. Wright, and P. H. Chappell, "Optical properties of human skin," *Journal of Biomedical Optics,* vol. 17, no. 9, p. 090901, 2012.

[15] M. Doi and S. Tominaga, "Spectral estimation of human skin color using the Kubelka-Munk theory," in *Color Imaging VIII: Processing, Hardcopy, and Applications*, 2003, vol. 5008: International Society for Optics and Photonics, pp. 221-228.

[16] J. V. Jokerst, A. J. Cole, D. Van de Sompel, and S. S. Gambhir, "Gold nanorods for ovarian cancer detection with photoacoustic imaging and resection guidance

via Raman imaging in living mice," *ACS Nano,* vol. 6, no. 11, pp. 10366-10377, 2012.

[17] M. Chen, T. Shaoheng, Z. Guo, X. Wang, S. Mo, X. Huang, G. Liu, and N. Zheng, "Core–Shell Pd@ Au Nanoplates as Theranostic Agents for *In-vivo* Photoacoustic Imaging, CT Imaging, and Photothermal Therapy," *Advanced Materials,* vol. 26, no. 48, pp. 8210-8216, 2014.

[18] K. Li and B. Liu, "Polymer-encapsulated organic nanoparticles for fluorescence and photoacoustic imaging," *Chemical Society Reviews,* vol. 43, no. 18, pp. 6570-6597, 2014.

[19] K. Pu, A. J. Shuhendler, J. V. Jokerst, J. Mei, S. S. Gambhir, Z. Bao, and J. Rao , "Semiconducting polymer nanoparticles as photoacoustic molecular imaging probes in living mice," *Nature Nanotechnology,* vol. 9, no. 3, pp. 233-239, 2014.

[20] Y. Zhang, J. Yu, A. R. Kahkoska, and Z. Gu, "Photoacoustic drug delivery," *Sensors,* vol. 17, no. 6, p. 1400, 2017.

[21] J. Kottmann, J. M. Rey, and M. W. Sigrist, "Mid-Infrared photoacoustic detection of glucose in human skin: towards non-invasive diagnostics," *Sensors,* vol. 16, no. 10, p. 1663, 2016.

[22] J. Y. Sim, C.-G. Ahn, E.-J. Jeong, and B. K. Kim, "*In-vivo* microscopic photoacoustic spectroscopy for non-invasive glucose monitoring invulnerable to skin secretion products," *Scientific Reports,* vol. 8, no. 1, pp. 1-11, 2018.

[23] Y. Cao, A. Kole, J. Hui, Y. Zhang, J. Mai, M. Alloosh, M. Sturek and J. X. Cheng, "Fast assessment of lipid content in arteries *in-vivo* by intravascular photoacoustic tomography," *Scientific Reports,* vol. 8, no. 1, pp. 1-10, 2018.

[24] J. Xia, J. Yao, and L. V. Wang, "Photoacoustic tomography: principles and advances," *Electromagnetic Waves (Cambridge, Mass.),* vol. 147, p. 1, 2014.

[25] Y. Zhou, J. Yao, and L. V. Wang, "Tutorial on photoacoustic tomography," *Journal of Biomedical Optics,* vol. 21, no. 6, p. 061007, 2016.

[26] P. K. Upputuri and M. Pramanik, "Recent advances toward preclinical and clinical translation of photoacoustic tomography: a review," *Journal of Biomedical Optics,* vol. 22, no. 4, p. 041006, 2016.

[27] A. Petschke and P. J. La Riviere, "Comparison of intensity-modulated continuous-wave lasers with a chirped modulation frequency to pulsed lasers for photoacoustic imaging applications," *Biomedical Optics Express,* vol. 1, no. 4, pp. 1188-1195, 2010.

[28] A. C. Tam, "Applications of photoacoustic sensing techniques," *Reviews of Modern Physics,* vol. 58, no. 2, p. 381, 1986.

[29] A. Demirkiran, A. Karakuzu, H. Erkol, H. Torun, and M. B. Unlu, "Analysis of microcantilevers excited by pulsed-laser-induced photoacoustic waves," *Optics Express,* vol. 26, no. 4, pp. 4906-4919, 2018.

[30] L. V. Wang and H.-i. Wu, *Biomedical optics: principles and imaging*. John Wiley & Sons, Hoboken, New Jersey, 2012.

[31] M. W. Schellenberg and H. K. Hunt, "Hand-held optoacoustic imaging: A review," *Photoacoustics,* vol. 11, pp. 14-27, 2018.

[32] L. ANSftSUo, "American national standard for the safe use of lasers," *American National Standards Institute. ANSIZ136. New York, NY: American National Standards Institute,* 2007.

[33] S. Liu, R. Zhang, Z. Zheng, and Y. Zheng, "Electromagnetic–acoustic sensing for biomedical applications," *Sensors,* vol. 18, no. 10, p. 3203, 2018.

[34] A. A. Oraevsky, S. L. Jacques, and F. K. Tittel, "Measurement of tissue optical properties by time-resolved detection of laser-induced transient stress," *Applied Optics,* vol. 36, no. 1, pp. 402-415, 1997.

[35] F. M. Hooi, O. Kripfgans, and P. L. Carson, "Acoustic attenuation imaging of tissue bulk properties with a priori information," *The Journal of the Acoustical Society of America,* vol. 140, no. 3, pp. 2113-2122, 2016.

[36] X. L. Deán-Ben, D. Razansky, and V. Ntziachristos, "The effects of acoustic attenuation in optoacoustic signals," *Physics in Medicine & Biology,* vol. 56, no. 18, p. 6129, 2011.

[37] C. Kim, T. N. Erpelding, K. I. Maslow, L. Jankovic, W. J. Akers, L. Song, S. Achilefu, J. A. Margenthaler, M. D. Pashley, and L. V. Wang, "Handheld array-based photoacoustic probe for guiding needle biopsy of sentinel lymph nodes," *Journal of Biomedical Optics,* vol. 15, no. 4, pp. 046010-046010-4, 2010.

[38] B. W. Zeff, B. R. White, H. Dehghani, B. L. Schlaggar, and J. P. Culver, "Retinotopic mapping of adult human visual cortex with high-density diffuse

optical tomography," *Proceedings of the National Academy of Sciences,* vol. 104, no. 29, pp. 12169-12174, 2007.

[39] D. Christensen, *Ultrasonic bioinstrumentation*. John Wiley & Sons, Hoboken, New Jersey, 1988.

[40] X. Deán-Ben and D. Razansky, "Optoacoustic signal excitation with a tone-burst of short pulses," *Photoacoustics,* vol. 11, pp. 1-5, 2018.

[41] P. Burgholzer, J. Bauer-Marschallinger, and M. Haltmeier, "Breaking the resolution limit in photoacoustic imaging using non-negativity and sparsity," *Photoacoustics,* vol. 19, p. 100191, 2020.

[42] A. Rosenthal, V. Ntziachristos, and D. Razansky, "Model-based optoacoustic inversion with arbitrary-shape detectors," *Medical Physics,* vol. 38, no. 7, pp. 4285-4295, 2011.

[43] D. Piras, C. Grijsen, P. Schütte, W. Steenbergen, and S. Manohar, "Photoacoustic needle: minimally invasive guidance to biopsy," *Journal of Biomedical Optics,* vol. 18, no. 7, pp. 070502-070502, 2013.

[44] G. Xu, S. A. Tomlins, J. Siddiqui, M. Davis, L. P. Kunju, J. T. Wei, and X. Wang, "Photoacoustic biopsy: a feasibility study," in *Optical Biopsy XIII: Toward Real-Time Spectroscopic Imaging and Diagnosis*, 2015, vol. 9318: International Society for Optics and Photonics, p. 931806.

[45] P. M. Phal, D. M. Brooks, and R. Wolfe, "Sonographically guided biopsy of focal lesions: a comparison of freehand and probe-guided techniques using a

phantom," *American Journal of Roentgenology,* vol. 184, no. 5, pp. 1652-1656, 2005.

[46] A. Garcia-Uribe, T. N. Erpelding, A. Krumholz, H. Ke, K. Maslow, C. Appleton, J. A. Margenthaler, and L. V. Wang, "Dual-modality photoacoustic and ultrasound imaging system for noninvasive sentinel lymph node detection in patients with breast cancer," *Scientific Reports,* vol. 5, no. 1, pp. 1-8, 2015.

[47] W. Xia, C. A. Mosse, R. J. Colchester, J. M. Mari, D. I. Nikitichev, S. J. West, S. Ourselin, P. C. Beard, and A. E. Desjardins, "Fiber optic photoacoustic probe with ultrasonic tracking for guiding minimally invasive procedures," in *European Conference on Biomedical Optics*, 2015: Optical Society of America, p. 95390K.

[48] Y. Cho, C. C. Chang, J. Yu, M. Jeon, C. Kim, L. V. Wang, and J. Zou, "Handheld photoacoustic tomography probe built using optical-fiber parallel acoustic delay lines," *Journal of Biomedical Optics,* vol. 19, no. 8, p. 086007, 2014.

[49] C. Kim, T. N. Erpelding, L. Jankovic, and L. V. Wang, "Performance benchmarks of an array-based hand-held photoacoustic probe adapted from a clinical ultrasound system for non-invasive sentinel lymph node imaging," *Philosophical Transactions of the Royal Society A: Mathematical, Physical and Engineering Sciences,* vol. 369, no. 1955, pp. 4644-4650, 2011.

[50] D. Cai, G. Li, D. Xia, Z. Li, Z. Guo, and S.-L. Chen, "Synthetic aperture focusing technique for photoacoustic endoscopy," *Optics Express,* vol. 25, no. 17, pp. 20162-20171, 2017.

[51] J.-M. Yang, C. Li, R. Chen, Q. Zhou, K. K. Shung, and L. V. Wang, "Catheter-based photoacoustic endoscope," *Journal of Biomedical Optics,* vol. 19, no. 6, p. 066001, 2014.

[52] A. Dangi, S. Agrawal, J. Lieberknecht, J. Zhang, and S.-R. Kothapalli, "Ring Ultrasound transducer based miniaturized photoacoustic imaging system," in *2018 IEEE SENSORS*, 2018, IEEE, pp. 1-4.

[53] T. Zhao, L. Su, and W. Xia, "Optical ultrasound generation and detection for intravascular imaging: a review," *Journal of Healthcare Engineering,* vol. 2018, 2018.

[54] A. Taruttis, A. C. Timmermans, P. C. Wouters, M. Kacprowicz, G. M. van Dam, and V. Ntziachristos, "Optoacoustic imaging of human vasculature: feasibility by using a handheld probe," *Radiology,* vol. 281, no. 1, pp. 256-263, 2016.

[55] L. Vionnet, J. Gateau, M. Schwarz, A. Buehler, V. Ermolayev, and V. Ntziachristos, "24-MHz scanner for optoacoustic imaging of skin and burn," *IEEE Transactions on Medical Imaging,* vol. 33, no. 2, pp. 535-545, 2013.

[56] R. J. Colchester, C. A. Mosse, D. I. Nikitichev, E. Z. Zhang, S. West, P. C. Beard, I. Papakonstantinou, and A. E. Desjardins, "Real-time needle guidance with photoacoustic and laser-generated ultrasound probes," in *Photons Plus Ultraosund: Imaging and Sensing* 2015*,* vol. 9323, pp. 932321-932321-5. International Society for Optics and Photonics, 2015

[57] C.-W. Wei, T.-M. Nguyen, J. Xia, B. Arnal, I. Pelivanov, and M. O'Donnell, "Clinically translatable ultrasound/photoacoustic imaging for real-time needle

biopsy guidance," in *2014 IEEE International Ultrasonics Symposium*, 2014, IEEE, pp. 839-842.

[58] J. L. Su, A. B. Karpiouk, B. Wang, and S. Y. Emelianov, "Photoacoustic imaging of clinical metal needles in tissue," *Journal of Biomedical Optics,* vol. 15, no. 2, p. 021309, 2010.

[59] E. Z. Zhang and P. C. Beard, "A miniature all-optical photoacoustic imaging probe," in *Photons Plus Ultrasound: Imaging and Sensing 2011*, 2011, vol. 7899, International Society for Optics and Photonics, p. 78991F.

[60] B. Chen, Y. Chen, and C. Ma, "Photothermally tunable Fabry-Pérot fiber interferometer for photoacoustic mesoscopy," *Biomedical Optics Express,* vol. 11, no. 5, pp. 2607-2618, 2020.

[61] A. B. Karpiouk, B. Wang, and S. Y. Emelianov, "Development of a catheter for combined intravascular ultrasound and photoacoustic imaging," *Review of Scientific Instruments,* vol. 81, no. 1, p. 014901, 2010.

[62] J. Hui, Y. Cao, Y. Zhang, A. Kole, P. Wang, G. Yu, G. Eakins, M. Sturek, W. Chen, and J. X. Cheng. "Real-time intravascular photoacoustic-ultrasound imaging of lipid-laden plaque in human coronary artery at 16 frames per second," *Scientific Reports,* vol. 7, no. 1, pp. 1-11, 2017.

[63] P. Wang, T. Ma, M. N. Slipchenko, S. Liang, J. Hui, K.K. Shung, S. Roy, M. Sturek, Q. Zhou, Z. Chen, and J. X. Cheng, "High-speed intravascular photoacoustic imaging of lipid-laden atherosclerotic plaque enabled by a 2-kHz barium nitrite raman laser," *Scientific Reports,* vol. 4, no. 1, pp. 1-7, 2014.

[64] M. Wu, K. Jansen, G. Springeling, A. F. van der Steen, and G. van Soest, "Impact of device geometry on the imaging characteristics of an intravascular photoacoustic catheter," *Applied Optics,* vol. 53, no. 34, pp. 8131-8139, 2014.

[65] J. Hui, Q. Yu, T. Ma, P. Wang, Y. Cao, R. S. Bruning, Y. Qu, Z. Chen, Q. Zhou, M. Sturek, and J. X. Cheng, "High-speed intravascular photoacoustic imaging at 1.7 μm with a KTP-based OPO," *Biomedical Optics Express,* vol. 6, no. 11, pp. 4557-4566, 2015.

[66] C. Fang, A. Ustun, Y. Cho, and J. Zou, "A charge amplification approach for photoacoustic tomography (PAT) with parallel acoustic delay line (PADL) arrays," *Measurement Science and Technology,* vol. 28, no. 5, p. 055108, 2017.

[67] I. L. Auerbach, J. P. Eckert, R. F. Shaw, and C. B. Sheppard, "Mercury delay line memory using a pulse rate of several megacycles," *Proceedings of the IRE,* vol. 37, no. 8, pp. 855-861, 1949.

[68] D. L. Arenberg, "Ultrasonic solid delay lines," *The Journal of the Acoustical Society of America,* vol. 20, no. 1, pp. 1-26, 1948.

[69] J. May, "Wire-type dispersive ultrasonic delay lines," *IRE Transactions on Ultrasonic Engineering,* vol. 7, no. 2, pp. 44-52, 1960.

[70] G. Boyd, L. Coldren, and R. Thurston, "Acoustic clad fiber delay lines," *IEEE Transactions on Sonics and Ultrasonics,* vol. 24, no. 4, pp. 246-252, 1977.

[71] I. Gelles, "Optical-Fiber Ultrasonic Delay Lines," *the Journal of the Acoustical Society of America,* vol. 39, no. 6, pp. 1111-1119, 1966.

[72] C.-C. Chang, Y. Cho, L. Wang, and J. Zou, "Micromachined silicon acoustic delay lines for ultrasound applications," *Journal of Micromechanics and Microengineering,* vol. 23, no. 2, p. 025006, 2012.

[73] Y. Cho, C. Chang, L. Wang, and J. Zou, "Micromachined silicon parallel acoustic delay lines as time-delayed ultrasound detector array for real-time photoacoustic tomography," *Journal of Optics,* vol. 18, no. 2, p. 024003, 2016.

[74] M. K. Yapici, C. Kim, C. C. Chang, M. Jeon, Z. Guo, X. Cai, J. Zou, and L. V. Wang, "Parallel acoustic delay lines for photoacoustic tomography," *Journal of Biomedical Optics,* vol. 17, no. 11, p. 116019, 2012.

[75] E. A. Lindgren, M. Rosen, and K. E. Amin, "Ultrasonic characterization of ceramic fibres at ambient and elevated temperatures," *Ultrasonics,* vol. 32, no. 6, pp. 411-419, 1994.

[76] B. A. Auld, *Acoustic fields and waves in solids*. Рипол Классик, John Wiley & Sons, 1973.

[77] T. Meeker, "Dispersive ultrasonic delay lines using the first longitudinal mode in a strip," *IRE Transactions on Ultrasonic Engineering,* no. 2, pp. 53-58, 1960.

[78] R. Gibson, "Solid ultrasonic delay lines," *Ultrasonics,* vol. 3, no. 2, pp. 49-61, 1965.

[79] C.-C. Chang, Y. Cho, and J. Zou, "A micromachined acoustic multiplexer for ultrasound and photoacoustic imaging applications," *Journal of Microelectromechanical Systems,* vol. 23, no. 3, pp. 514-516, 2014.

[80] Y. Cho, A. Kumar, S. Xu, and J. Zou, "Micromachined silicon acoustic delay line with 3D-printed micro linkers and tapered input for improved structural stability and acoustic directivity," *Journal of Micromechanics and Microengineering,* vol. 26, no. 10, p. 105003, 2016.

[81] A. K. Ustun and J. Zou, "A photoacoustic sensing probe using optical fiber acoustic delay line," *Photoacoustics,* vol. 13, pp. 18-24, 2019.

[82] A. Ustun and J. Zou, "A novel photoacoustic sensing probe using optical fiber acoustic delay line," in *Photons Plus Ultrasound: Imaging and Sensing 2018*, 2018, vol. 10494: International Society for Optics and Photonics, p. 104946F.

[83] K. Cheng, H. L. Chan, C. Choy, Q. Yin, H. Lu, and Z. Yin, "Piezoelectric coefficients of PMN-0.33 PT single crystals," in *Applications of Ferroelectrics, 2000. ISAF 2000. Proceedings of the 2000 12th IEEE International Symposium on*, 2000, vol. 2, IEEE, pp. 533-536.

[84] H. J. Lee, S. Zhang, J. Luo, F. Li, and T. R. Shrout, "Thickness-Dependent Properties of Relaxor-PbTiO3 Ferroelectrics for Ultrasonic Transducers," *Advanced Functional Materials,* vol. 20, no. 18, pp. 3154-3162, 2010.

[85] H. Jiang, Y. K. Zou, Q. Chen, K. K. Li, R. Zhang, Y. Wang, H. Ming, and Z. Zheng, "Transparent electro-optic ceramics and devices," in *Optoelectronic Devices and Integration*, 2005, vol. 5644: International Society for Optics and Photonics, pp. 380-395.

[86] M. D. Benoy, E. M. Mohammed, M. Suresh Babu, P. J. Binu, and B. Pradeep, "Thickness dependence of the properties of indium tin oxide (ITO) FILMS

prepared by activated reactive evaporation," *Brazilian Journal of Physics,* vol. 39, no. 4, 2009.

[87] X. Wan, H. Luo, and X. Zhang and X. Zhao, "Feasibility of Growing and Optical Properties of Ferroelectric," *Trends in Crsytal Growth Research,* Book Chapeter p. 45, 2005.

[88] B. Lengenfelder, F. Mehari, M. Hohmann, M. Heinlein, E. Chelales, M. J. Waldner, F. Klämpfl, Z. Zalevsky, and M. Schmidt, "Remote photoacoustic sensing using speckle-analysis," *Scientific Reports,* vol. 9, no. 1, pp. 1-11, 2019.

[89] A. K. Ustun and J. Zou, "A Photoacoustic Sensing Probe Using Single Optical Fiber Acoustic Delay Line," *IEEE Sensors Journal,* vol. 19, no. 19, pp. 8714-8719, 2019.

[90] E. M. Strohm, M. J. Moore, and M. C. Kolios, "Single cell photoacoustic microscopy: a review," *IEEE Journal of Selected Topics in Quantum Electronics,* vol. 22, no. 3, pp. 137-151, 2015.

[91] T. Zhao, A. E. Desjardins, S. Ourselin, T. Vercauteren, and W. Xia, "Minimally invasive photoacoustic imaging: Current status and future perspectives," *Photoacoustics,* vol. 16, p. 100146, 2019.

[92] A. H. Meitzler, "Ultrasonic delay lines for digital data storage," *IRE Transactions on Ultrasonic Engineering,* vol. 9, no. 2, pp. 30-37, 1962.

[93] J. Eveleth, "A survey of ultrasonic delay lines operating below 100 Mc/s," *Proceedings of the IEEE,* vol. 53, no. 10, pp. 1406-1428, 1965.

[94] T. Moriya, Z. Hu, and Y. Tanahashi, "Development of flexible acoustic transmission line for intravascular ultrasonography," in *2000 IEEE Ultrasonics Symposium. Proceedings. An International Symposium (Cat. No. 00CH37121)*, 2000, vol. 2, IEEE, pp. 1227-1230.

[95] I. Steinberg, D. M. Huland, O. Vermesh, H. E. Frostig, W. S. Tummers, and S. S. Gambhir, "Photoacoustic clinical imaging," *Photoacoustics,* vol. 14, pp. 77-98, 2019.

[96] A. Sarvazyan and S. Tsyuryupa, "Potential biomedical applications of non-dissipative acoustic radiation force," in *Proceedings of Meetings on Acoustics 171ASA*, 2016, vol. 26, no. 1, Acoustical Society of America, p. 020002.